

# Extreme-mass ratio inspirals in Schwarzschild - de Sitter spacetime I: Weak-field orbits

John Adrian N. Villanueva<sup>1</sup> and Ian Vega

National Institute of Physics, University of the Philippines Diliman 1101, Quezon City, Philippines

E-mail: [javillanueva@nip.upd.edu.ph](mailto:javillanueva@nip.upd.edu.ph)

**Abstract.** The inspiral of a compact object into a black hole is a key source of low-frequency gravitational waves for future space-based detectors like LISA. While models of this process have advanced, they typically focus on asymptotically flat spacetimes. In this paper, we explore how the absence of asymptotic flatness affects the slow, adiabatic orbital evolution due to radiation reaction. This lack of asymptotic flatness can arise from external environments or an expanding universe. Using the Schwarzschild-de Sitter (SdS) spacetime, where the deviation from flatness is governed by the cosmological constant, we study bound orbits characterized by their semi-latus rectum  $p$  and eccentricity  $e$ . We calculate how the cosmological constant shifts the separatrix between bound and plunging orbits and alters the relationship between the binary's binding energy, angular momentum, and orbital parameters. Assuming the orbital timescale is much shorter than the inspiral timescale, we apply a modified quadrupole formula to examine the impact of a small positive cosmological constant on the orbital evolution in the weak-field limit. We find that the cosmological constant accelerates the decrease in eccentricity, reducing inspiral plunge times, which could influence event rate estimates for space-based detectors.

---

## Contents

<b>1</b>	<b>Introduction</b>	<b>1</b>
<b>2</b>	<b>Orbital mechanics in Schwarzschild-de Sitter spacetime</b>	<b>4</b>
2.1	Timelike geodesics in Schwarzschild-de Sitter spacetime	5
2.2	Bound orbits in Schwarzschild-de Sitter	5
2.3	Separatrices for bound orbits	8
2.3.1	Plunging separatrix	9
2.3.2	Scattering separatrix	11
<b>3</b>	<b>Adiabatic orbital evolution</b>	<b>13</b>
3.1	Evolution of circular orbits	16
3.2	Evolution of eccentric orbits	18
3.3	Inspiral, circularization and orbital trajectory	20
<b>4</b>	<b>Gravitational waveforms</b>	<b>27</b>
4.1	Orbits near the separatrix	28
4.2	Orbits far away from the separatrix	30
<b>5</b>	<b>Timescales for gravitational wave detection</b>	<b>35</b>
<b>6</b>	<b>Conclusions</b>	<b>38</b>

---

## 1 Introduction

Gravitational waves have emerged as powerful probes of the universe, opening a fundamentally new window onto its most energetic and previously inaccessible phenomena. The recent direct detections of gravitational-wave signals [1] have firmly established their role as essential tools in modern astrophysics. Together with solar and supernova neutrinos, diffuse gamma-ray backgrounds, and electromagnetic counterparts in binary neutron star mergers [2, 3]—gravitational waves form an additional pillar of multimessenger astronomy. By enabling us to “hear” the gravitational dynamics of compact objects, they reveal aspects of the cosmos that were once beyond observational reach, transforming our understanding of an otherwise silent universe.

Gravitational wave astronomy could also help cosmology on the problem of the expansion of the universe [4]. The general rate of expansion, known as the Hubble parameter [5, 6] is closely related to the cosmological constant,  $\Lambda$ . While estimates of this parameter have been obtained, most notably by the Planck collaboration [7], this will still be tested more thoroughly using gravitational wave signals [8]. Borrowing the idea of standard candles from stars to determine the gravitational redshift distance between celestial bodies, standard sirens have also been put forward for gravitational wave sources [9–11]. Relevant sources include black hole binary mergers [12] and neutron star binaries [13], both of which have already been observed by the ground-based triple gravitational wave interferometer network consisting of LIGO (Hanford and Livingston) and Virgo (Italy). The types and number of sources available for analysis will increase significantly with the upcoming launch of the space-based LISA (Laser Interferometer Space Antenna) gravitational wave detector [14–17].

Both ground-based and future space-based detectors will be pivotal in analyzing gravitational wave signals to estimate the Hubble parameter and the size of the universe. Low-frequency gravitational wave sources, particularly in the millihertz range, will be key targets for space-based detectors like LISA. Extreme-mass ratio inspirals (EMRIs) [18, 19] in particular, where compact objects spiral into massive black holes with a mass ratio of approximately  $10^{-6}$ , are expected to have large number of gravitational wave cycles within the millihertz band (typically on the order of the inverse of the mass ratio) which should enable us to precisely probe strong-field gravitational effects [20, 21].

One could envision an EMRI as a binary system containing a stellar-mass compact object, and a supermassive black hole. However, the typical isolated two-body problem in classical physics provides an idealized model of a celestial binary system, neglecting various external physical factors in a real astrophysical context. To accurately model the motion of such a binary, one must account for physically realistic external agents that contribute gravitationally. These external influences are often referred to as environmental effects, and have been extensively discussed in the literature [22–25].

In addition to the effects of matter [26–29] and external fields [30, 31], we argue that the expansion of spacetime itself can also be considered an environmental effect. While there have been numerous studies on the radiation reaction in binary systems, fewer have focused on the influence of the expanding universe on binary dynamics [32, 33]. The inclusion of the cosmological constant not only means that the spacetime has a constant acceleration of expansion, it adds new features in the spacetime geometry [34] such as the emergence of a cosmological horizon and new properties to the geodesics of the spacetime, as studied thoroughly in [35] and [36].

The de Sitter solution, which provides the simplest description of an expanding universe, generates a nontrivial gravitational flux that can be detected at infinity due to spacetime curvature. This phenomenon has been rigorously examined by [32, 37–46]. When a black hole binary is placed within an expanding universe, the resulting spacetime is modeled as Schwarzschild-de Sitter, also known as Kottler spacetime [47]. This solution represents the simplest black hole solution to Einstein’s field equations that includes a cosmological constant [34].

The objective of this work is to investigate the impact of spacetime expansion due to the cosmological constant on an inspiraling binary system, building on the energy and angular momentum flux formulas provided by [33]. We focus on the orbital evolution of binaries primarily driven by gravitational wave radiation and its associated radiation reaction. Specifically, we consider a binary consisting of a stellar-mass compact object gravitationally bound to a black hole, such as an EMRI. We assume that the compact object survives tidal disruption by the Schwarzschild black hole, allowing it to successfully inspiral and eventually plunge. The binary is placed within a de Sitter universe, which expands at a constant rate. As a result, outside the black hole, the spacetime is effectively described by the Schwarzschild-de Sitter metric. In this framework, we analyze both conservative and dissipative effects of the cosmological constant on the binary’s dynamics.

To provide a comprehensive description, we consider generic orbits with eccentricities ranging from  $e = 0$  (circular orbits) to  $e = 1$  (unbound orbits), treating eccentricities approaching unity as representing unbound orbits. Although [33] have already examined the effect of radiation on orbital evolution in de Sitter space, they did not modify the full Keplerian dynamical quantities to include the de Sitter terms nor fully explore how the cosmological constant affects orbital dynamics. In this work, we extend their analysis by providing a com-

plete treatment of the weak-field, adiabatic dissipative dynamics driven by radiation reaction for a compact binary. We also present preliminary results on strong-field energy fluxes, offering a check on the validity of the weak-field flux approximations. Additionally, we explore other conservative effects of the cosmological constant on the binary, such as the separatrix and the parameters of the last stable orbit, as well as the influence of radiation reaction on the periapsis advance, which is also modulated by the cosmological constant. Moreover, we calculate adiabatic waveforms for a continuously evolving orbit due to radiation reaction in Schwarzschild-de Sitter spacetime, highlighting shifts in the waveform's amplitude and phase.

We estimate the impact of a realistic cosmological constant, placing particular emphasis on its role in the dissipative dynamics driven by gravitational radiation reaction. While the contribution from  $\Lambda$  is generally subdominant relative to leading post-Newtonian effects, its relative importance increases near the in certain regions of the parameter space (which will be discussed below), where it may approach the magnitude of post-Newtonian corrections. More broadly, our results may be interpreted in terms of an environmental contribution to the gravitational potential of the form  $\delta V \sim \Lambda r^2$ . In this sense,  $\Lambda$  serves as a proxy for an  $r^2$  perturbation to the effective potential.

An example arises in studies of accretion or tidal interactions in a binary system analyzed in the co-rotating frame. In this setting, the Roche potential contains an additional contribution associated with the binary's angular velocity  $\omega$ , including terms that scale as  $\sim (\omega \times r)^2$  [48]. Our results may therefore be mapped onto such systems by interpreting a large effective cosmological constant  $\Lambda$  as corresponding to a large orbital angular velocity induced from a Coriolis force. Similarly, the framework developed here could be extended to describe an EMRI embedded in an external uniform magnetic field, where the magnetic-field contribution to the metric functions scales as  $\sim Br^2$  [49, 50]. In this way, the present analysis captures a broader class of physical scenarios characterized by quadratic modifications to the effective gravitational potential.

The paper is divided into five parts. Section 2 contains an elementary review of bound timelike geodesics in Schwarzschild-de Sitter spacetime, which represents the conservative trajectories followed by particles. We parametrize bound orbits using either their energy and angular momentum  $(E, L)$  or their semilatus rectum and eccentricity  $(p, e)$ . An important result of this section is the effect of the cosmological constant on the separatrix surface, the boundary in parameter space separating unstable and stable bound orbits. In Section 3, we build on the results of Hoque and Aggarwal to describe the influence of the cosmological constant on orbital evolution due to radiation reaction in the weak-field, adiabatic limit. We check the accuracy of these results with a preliminary calculation of the fluxes derived from black hole perturbation theory in Schwarzschild-de Sitter spacetime. Additionally, we provide sample orbital shapes to illustrate the impact of the cosmological constant on the dynamics of the binary system. Section 4 focuses on the calculation of adiabatic waveforms, demonstrating how the cosmological constant modifies the amplitude and phase of gravitational waveforms for both circular and eccentric binaries. We also explore the constraints that the adiabatic approximation places on the mass ratios and the cosmological constant, determining the conditions under which these approximations remain valid. Lastly, in Section 5 we investigate the effect of the cosmological constant on the plunge times of generic orbits and examine how this relates to the timescales for detecting gravitational wave sources.

We adopt the usual conventions by Misner, Thorne and Wheeler, which uses the mostly plus metric signature and the geometrized units of naturalizing the constants  $G = c = 1$ . For astrophysical applications, these naturalized constants applied to conventional units translate

to  $1 M_\odot \simeq 5 \times 10^{-6}$  s  $\simeq 1.5$  km and  $1 \text{ pc} \simeq 10^8$  s.

## 2 Orbital mechanics in Schwarzschild-de Sitter spacetime

The first exact solution to the Einstein field equation representing a black hole immersed in an expanding universe is known as the Schwarzschild-de Sitter (SdS) solution [51]:

$$g_{\mu\nu} = \text{diag}(-f(r), f(r)^{-1}, r^2, r^2 \sin^2 \theta), \quad (2.1)$$

where we have the metric function,  $f(r) = 1 - 2M/r - \Lambda r^2/3$ . This metric is a special case of the McVittie solution [52], for positive spatial curvature and a constant Hubble parameter,  $H(t) = H_0$ . The SdS metric satisfies the vacuum Einstein field equation with a positive cosmological constant,  $\Lambda$ :

$$G_{\mu\nu} - \Lambda g_{\mu\nu} = T_{\mu\nu} = 0. \quad (2.2)$$

When  $0 < \Lambda < \Lambda_{\max} := (3M)^{-2}$  (or  $1/\sqrt{\Lambda} > 3M$ ), the spacetime will feature two horizons (i.e. the roots of equation (2.1)): the event horizon, which marks the boundary of a black hole, and the cosmological horizon, which sets the scale of the observable universe. When  $\Lambda > (3M)^{-2}$ , the spacetime is not static for any  $r$  (i.e. there no longer exists a static patch), and the SdS spacetime is no longer a good representation of a black hole immersed in an expanding universe. We shall only be interested in the former case, and we will focus on orbits between the event horizon and cosmological horizon.

It is convenient to use dimensionless variables  $\tilde{r} := r/M$  and  $\lambda := M^2\Lambda/3$ . For both horizons to exist, as we required in the preceding paragraph, we thus require  $\lambda < \lambda_{\max} := 1/27$ . A value of  $\lambda$  approaching this critical value would imply an unrealistic scenario in which a black hole is comparable in size to the entire universe. Based on our best estimates for the cosmological constant and the Hubble parameter [53], we instead find that  $\lambda \ll 1$ . For a supermassive black hole (SMBH) of mass  $M = 10^6 M_\odot$  and  $\Lambda = 10^{-50} \text{ km}^{-2}$ , our dimensionless cosmological constant  $\lambda$  is of order  $\lambda = 10^{-38}$ . This is an extraordinarily small number, leading us to expect that any resulting effects from  $\lambda$  will be practically negligible. Nonetheless, we find it worthwhile to explore the potential effects when  $\lambda$  is not exceedingly small, as this may serve as a proxy for other environmental factors with similar  $r^2$ -scaling in the effective potential [54]. Sticking to a cosmological constant scenario, we note that a non-negligible  $\lambda = 10^{-5}$ , for  $\Lambda \sim 10^{-50} \text{ km}^{-2}$ , would imply a black hole mass of  $M \approx 10^{22} M_\odot$ .

We are thus fully justified in exploiting  $\lambda \ll 1$  as a small parameter in all of our calculations. As an example, consider the locations of the horizons, which are obtained by solving for the roots of the metric function:

$$f(\lambda; r) = 1 - \frac{2}{r} - \lambda r^2 = 0. \quad (2.3)$$

Up to  $\mathcal{O}(\lambda^2)$ , the roots are

$$r_h = 2 + 8\lambda + \mathcal{O}(\lambda^2) \quad (2.4)$$

$$r_c = -1 + \lambda^{-1/2} - \frac{3}{2}\lambda^{1/2} - 4\lambda + \mathcal{O}(\lambda^2) \quad (2.5)$$

$$r_o = -1 - \lambda^{-1/2} + \frac{3}{2}\lambda^{1/2} - 4\lambda + \mathcal{O}(\lambda^2) \quad (2.6)$$

with  $r_h$  as the horizon of the SdS black hole,  $r_c$  as the cosmological horizon and  $r_o$  as an unphysical negative root. We further see that requiring that the black hole is inside the universe,  $r_h < r_c$ , implying  $\lambda \lesssim 0.06$ , satisfies the stricter condition  $\lambda < \lambda_{\max} := 1/27$ .

## 2.1 Timelike geodesics in Schwarzschild-de Sitter spacetime

Test particles with mass  $\mu$  move along timelike geodesics. In any static and azimuthally symmetric spacetime, geodesics will possess conserved quantities

$$\xi_t u^t = -f(r) \frac{dt}{d\tau} = \tilde{E}/\mu \quad (2.7)$$

$$\eta_\phi u^\phi = r^2 \sin^2(\theta) \frac{d\phi}{d\tau} = \tilde{L}/\mu, \quad (2.8)$$

which are associated with the timelike and azimuthal Killing vectors,  $\xi^\mu$  and  $\eta^\mu$ , respectively. The conserved quantities may be interpreted as the energy and angular momentum conserved during time translation and azimuthal translation of a particle. Inserting Eqs. (2.7) and (2.8) into the normalization condition of the four-velocity,  $u^\mu u_\mu = -1$ , we obtain a radial equation of motion familiar from elementary orbital mechanics:

$$\left( \frac{dr}{d\tau} \right)^2 = \tilde{E}^2 - V_{\text{eff}}(\tilde{L}, \lambda; r), \quad V_{\text{eff}}(\tilde{L}, \lambda; r) = f(\lambda; r) \left( 1 + \frac{\tilde{L}^2}{r^2} \right). \quad (2.9)$$

The equation is uniquely characterized by an “effective” potential,  $V_{\text{eff}}$ . In the SdS spacetime, the shape of the effective potential  $V_{\text{eff}}$  depends on parameters  $(\tilde{L}, \lambda)$ . More complete treatments of geodesics in the SdS spacetime can be found in [34, 36, 55].

## 2.2 Bound orbits in Schwarzschild-de Sitter

Bound orbits in static and spherically symmetric spacetimes are typically described by their energy and angular momentum. Another common and often more informative parametrization of bound orbits uses orbital parameters [56], such as the semi-latus rectum,  $p$ , and eccentricity,  $e$ . One imagines an “instantaneous” (or osculating) Keplerian orbit

$$r(\psi) = \frac{p m}{1 + e \cos \psi}, \quad (2.10)$$

representing the true trajectory. Here,  $m = m_1 + m_2$  is the total mass of the orbiter (with mass  $m_1$ ) and the central object (with mass  $m_2$ ) in a reduced two-body problem. The true anomaly,  $\psi$ , is the angle swept by the orbiter around the central object, accounting for the argument  $\delta$  at the periapsis. The coordinate azimuthal angle  $\phi$  thus equals  $\phi = \psi + \delta$ . For this paper we will be considering a compact object-black hole (CO-BH) system with reduced mass  $\mu = m_1 m_2 / m$ . This parametrization is particularly useful when studying processes that induce slow changes in the energy and angular momentum, such as radiation reaction. In this context, the adiabatic evolution can be pictured as a continuous sequence of Keplerian orbits of different sizes and shapes.

For a CO-BH system with the compact object much smaller than the central black hole (EMRI), the reduced mass will be approximately equal to the mass of the compact object solely,  $\mu = \mu_{CO}$ , and the total mass will be approximately equal to mass of the black hole,  $m = M_{BH} = M$ . We shall rescale  $r$  in Eq. ((2.10)) by the total mass, i.e.  $r \rightarrow r/M$ , henceforth.

The transformation from  $(\tilde{E}, \tilde{L})$  to  $(p, e)$  is obtained starting with the orbit equation

$$\left( \frac{1}{r^2} \frac{dr}{d\phi} \right)^2 = \frac{1}{\tilde{L}^2} \left( \tilde{E}^2 - V_{\text{eff}} \right). \quad (2.11)$$

A bound orbit will have two turning points,  $r_a$  and  $r_p$ , respectively corresponding to the maximum (apoapsis) and minimum distance (periapsis) of the small compact object from the black hole. The radial equation of motion, Eq. (2.9), evaluated at the two turning points  $r = r_{a(p)}$  gives us two algebraic equations that can be solved for  $(\tilde{E}, \tilde{L})$ , giving expressions in terms of  $(r_a, r_p)$ . In turn,  $r_a$  and  $r_p$  can be expressed in terms of  $p$  and  $e$  using Eq. ((2.10)):

$$r_a = \max[r(\psi)] = r(\psi = \pi) = p(1 - e)^{-1} \quad (2.12)$$

$$r_p = \min[r(\psi)] = r(\psi = 0) = p(1 + e)^{-1}. \quad (2.13)$$

For the Schwarzschild metric, one can work out explicit expressions for  $(\tilde{E}(r_a, r_p), \tilde{L}(r_a, r_p))$  in terms of  $(p, e)$ . However, for the more complicated SdS metric, this procedure does not yield explicit expressions. Recognizing that the cosmological constant is small, we shall content ourselves with working out approximate expressions valid only to first order in  $\Lambda$ . In terms of the scaled radial variable  $r \rightarrow r/M$  and scaled cosmological constant  $\lambda \rightarrow (1/3)M^2\Lambda$ , the conserved quantities are given by:

$$L^2 = \left( \frac{p^2}{p - 3 - e^2} \right) \left( 1 - \lambda \frac{p^3}{(1 - e^2)^2} + \mathcal{O}(\lambda^2) \right), \quad (2.14)$$

$$E^2 = \left( \frac{1}{p} \frac{(p-2)^2 - 4e^2}{p - 3 - e^2} \right) \left( 1 - \lambda \frac{p^3}{(p-2)^2 - 4e^2} \frac{(p-2 + (p-6)e^2)}{(e^2 - 1)^2} + \mathcal{O}(\lambda^2) \right), \quad (2.15)$$

where we have similarly non-dimensionalized the energy and angular momentum according to  $E^2 \rightarrow (\tilde{E}/\mu)^2$  and  $L \rightarrow (\tilde{L}/M\mu)$ .

We note that the above construction of the parameter transformation forbids us from including circular orbits  $e = 0$ . Even though the resulting expressions  $E(p, e)$  and  $L(p, e)$  are regular in the limit  $e \rightarrow 0$ , two distinct bound turning points (equations (2.12) and (2.13) which loses meaning at  $e \rightarrow 0$ ) are required to keep the transformation  $(E(r_a, r_p), L(r_a, r_p)) \rightarrow (E(p, e), L(p, e))$  defined, thus restricting the eccentricity to be within  $0 < e < 1$ .

The effect of the cosmological constant on the energy and angular momentum can be understood more clearly if we translate the equations in terms of the classical solutions to the Keplerian two-body problem. Expressing the energy equation in terms of the Newtonian binding energy  $\varepsilon = (E^2 - 1)/2$ , we get the cosmological corrections for weak-field slow-moving orbits:

$$L^2 = p - \lambda \frac{p^4}{(1 - e^2)^2} + O(\lambda^2 p^3) \quad (2.16)$$

$$\varepsilon = -\frac{1 - e^2}{2p} - \lambda \frac{(e^2 + 1) p^2}{(1 - e^2)^2} + O(\lambda^2 p). \quad (2.17)$$

The relations above can be used to put limits on the possible orbital parameters of bound orbits in SdS. We see from these equations that the cosmological constant makes the binding energy of an orbit more negative, making more eccentric orbits tighter, while decreasing the angular momentum required to reach a certain eccentricity value. We see therefore that bound orbits in a  $\lambda > 0$  spacetime require more energy input to separate. Looking at the angular momentum in equation (2.16), and requiring it to be always positive along with  $p$ , we could also limit the possible values of the eccentricity of an orbit. A particular SdS orbit

can therefore only have eccentricity values,  $0 < e < 1 - \sqrt{\lambda}p^{3/2}$ . These effects becomes more pronounced at higher eccentricities due to the  $(1 - e^2)$  singular factor.

We can also get the Newtonian limit of geodesics in the SdS spacetime. In isotropic coordinates  $\{T, R, \theta, \phi\}$ , the areal radius  $r$  is related to the isotropic radius  $R$  by the function

$$r = R \left[ \left( 1 + \frac{M}{2R} \right)^2 + \Lambda \frac{R^2}{4} \left( 1 + \frac{2M}{R} \right) \right] + \mathcal{O}(\Lambda^2) \quad (2.18)$$

and the SdS line element up to leading order in  $\Lambda$  is

$$ds^2 = -A(R)^2 dT^2 + B(R)^2 (dR^2 + R^2 d\Omega^2), \quad (2.19)$$

with the metric functions

$$A(R)^2 = \left( \frac{1 - \frac{M}{2R}}{1 + \frac{M}{2R}} \right)^2 - \frac{\Lambda}{3} \left( R^2 \left( 1 + \frac{M}{2R} \right)^4 - \frac{MR}{2} \left( \frac{1 + \frac{2M}{R}}{(1 + \frac{M}{2R})^4} \right) \right) + \mathcal{O}(\Lambda^2) \quad (2.20)$$

$$B(R)^2 = \left[ \left( 1 + \frac{M}{2R} \right)^2 + \frac{\Lambda R^2}{12} \left( 1 + \frac{2M}{R} \right) \right]^2 + \mathcal{O}(\Lambda^2) \quad (2.21)$$

and  $d\Omega^2$  as the metric on the unit 2-sphere. Note that we have brought back the dimensional parameters  $(M, \Lambda)$ , which means that the coordinate  $R$  has units of length.

We consider the region simultaneously far from the black hole event horizon and the cosmological horizon, i.e.  $2M \ll R \ll \Lambda^{-1}$ , which we assume to exist because  $2M \ll \Lambda^{-1}$ .

In this region, the metric components are that of Minkowski with corrections:

$$g_{00} = -1 + \frac{2M}{R} + \frac{\Lambda}{3} R^2 \left( 1 + \frac{5M}{2R} \right) + \mathcal{O}(\Lambda^2) + \mathcal{O} \left( \frac{2M}{R} \right)^2 \quad (2.22)$$

$$g_{jk} = \delta_{jk} \left( 1 + \frac{2M}{R} - \frac{\Lambda}{3} R^2 \left( \frac{1}{2} + \frac{3M}{2R} \right) \right) + \mathcal{O}(\Lambda^2) + \mathcal{O} \left( \frac{2M}{R} \right)^2. \quad (2.23)$$

The spatial acceleration of a free-falling particle can then be calculated to be

$$\begin{aligned} \frac{dv^j}{dT} &= \partial_j U + \frac{\Lambda}{3} \left[ R + \frac{1}{2} U + \frac{7}{4} R^2 \partial_j U - \frac{v^2}{2} (R + 8RU + 4R^2 \partial_j U) \right] \\ &\quad + \mathcal{O}(\Lambda^2) + \mathcal{O} \left( \frac{2M}{R} \right)^2 \end{aligned} \quad (2.24)$$

which shows the Newtonian spatial acceleration with a potential,  $U = 2M/R$ , along with the leading order correction due to the cosmological constant.

Finally, we show how constant  $(p, e)$  curves lives in the  $(E, L)$  space and vice versa both in Schwarzschild and SdS in Figure 1a and 1b. We show in Figure 1a the constant  $p$  and  $e$  curves in the  $(E, L)$  space under the constraint of the separatrices that will be covered in the next subsection. The  $e = 0$  curve serves as a lower boundary for the possible  $(E, L)$  for a bound orbit. In Figure 1b we show the constant  $E$  and  $L$  curves in  $(p, e)$  space. We see here that as we approach the  $e = 0$  limit, the  $(E, L)$  curves become parallel to each other restricting the mapping of the  $(p, e)$  to  $(E, L)$  transformation. We show this further

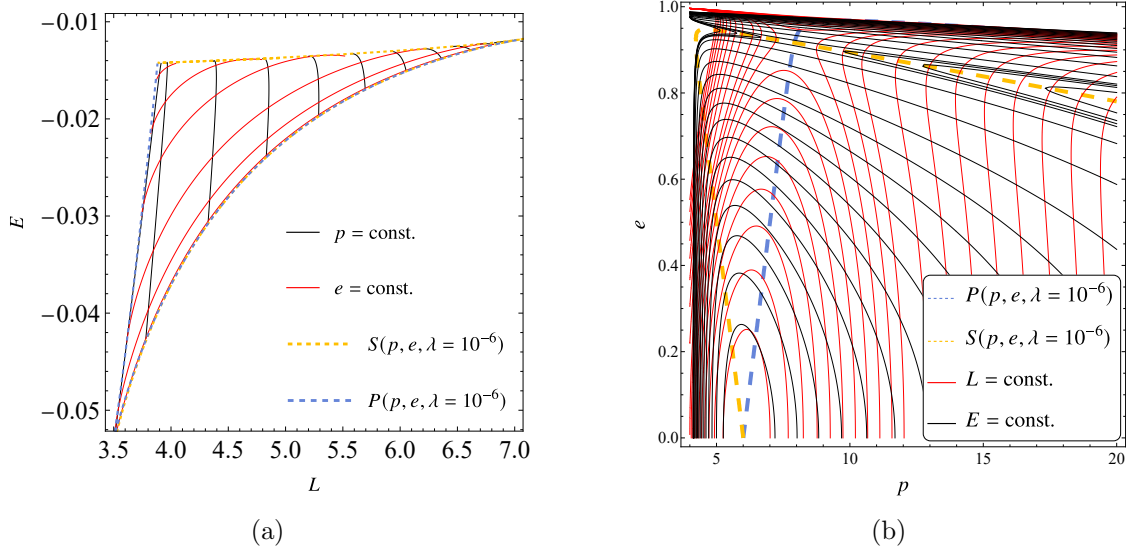


**Figure 1:** (a) Constant  $p$  and  $e$  curves in SdS  $(E, L)$  space with black lines as constant  $p$  curves increasing to the right and red lines as constant  $e$  curves increasing upwards. (b) Constant  $E$  (black) and  $L$  curves (red) in  $(p, e)$  space in SdS spacetime. The dashed curves are the separatrices (equation (2.26) and equation (2.30)) of bound orbits or the curves where the determinant of the Jacobian of transformation from  $(p, e) \rightarrow (E, L)$  becomes zero.

analytically by looking at the points where the Jacobian becomes degenerate or when the determinant of the transformation becomes zero. The transformation  $(E, L) \rightarrow (p, e)$  is facilitated by the matrix  $J_{ij}$  wherein  $J_{ij} = \partial_i \rho_j$  with  $i$  referring to the elements of  $(p, e)$  and  $\rho_j$  referring to the elements of  $(E, L)$ . The zeroes of the determinant  $|J_{ij}| = 0$  is located at  $e = 0$  as well as in regions that will be shown to be the separatrices  $p_{\text{inner}}$  and  $p_{\text{outer}}$  in the  $(p, e)$  space which will be discussed in Section 2.3. This shows that the transformation breaks down at these regions.

### 2.3 Separatrices for bound orbits

Compact binaries serve as sources of continuous gravitational wave signals during their inspiral phase, ending the signal at the merger and ringdown. It would then be relevant to reduce the  $(p, e)$  parameter space and further the  $(L, E)$  parameter space into those that will be bound orbits and separate them from the unbound orbital parameters that are either plunging or scattering trajectories.

Although the position of the last stable orbit (LSO) in Schwarzschild spacetime is already textbook knowledge found in many core general relativity books [57–59], the position in the full orbital parameter space (not only for  $e = 0$ ) is only a recent finding. For generic orbits in Schwarzschild, a paper by Poisson et al. [56] derived the fundamental  $p = 6 + 2e$  curve for marginally stable orbits. This curve however will be modified as a spacetime obtains other parameters. For rotating black hole spacetimes like the Kerr, numerical approximations of this separatrix are sufficient [60] but a more recent work obtained an analytic expression [61–63]. For charged black holes, the innermost stable circular orbit [64] and sufficient conditions for the position of marginally stable orbits has been derived [65, 66] but a generalized expression for the last stable orbit is yet to be found. In spacetimes with a cosmological

constant, a paper by [34, 35, 67] and more recently with an added contribution of a spin from [68] presented the condition for marginally stable generic orbits.

As discussed briefly in the last subsection (Section 2.2), the zeroes of the Jacobian of the transformation  $(E, L) \rightarrow (p, e)$  coincides with what we will be calling the *separatrix curves* for bound and unbound orbits in the  $(p, e)$  space. We will show two kinds of separatrices which will be a feature of the SdS orbital dynamics. The usual separatrix in the Schwarzschild spacetime is a plunging separatrix in which orbital parameters outside of the region bounded by the curve leads eventually to plunging orbits. We show in this section a scattering separatrix wherein orbital parameters outside the region bounded by this curve will lead to a scattering orbit up to infinity. We show the conventional way to derive these curves in this section which is to analyze the family of points that merges the turning points with the unstable maximas in the effective potential. Alternatively, the separatrix polynomials can also be derived by finding the zeroes of the Jacobian of the transformation  $(E, L) \rightarrow (p, e)$  which means that at the separatrix itself, the orbital parameters will not be valid to describe the dynamics of the orbit anymore.

### 2.3.1 Plunging separatrix

In this part, we show a representation of the plunging separatrix curve, or the location of the last stable orbit (LSO), of marginally bound orbits in  $(p, e)$  space to show at which point in the parameter space is the region of orbital plunge. The locus of all parameter values that will create a merged plunge and bound region in the effective potential will be the plunging separatrix in the  $(p, e, \lambda)$  parameter space. The maxima of the potential must be located at the periapsis, and is expressed mathematically as [63]:

$$\frac{dV_{\text{eff}}}{dr} \Big|_{r=r_p} = 0. \quad (2.25)$$

This method of deriving the separatrix means that we are considering that at the periapsis,  $r = r_p = p(1 + e)^{-1}$ , the bound orbiter will be marginally stable and thus will either plunge or scatter away depending on the evolution of the orbit. Together with the energy and angular momentum for bound orbits (equation (2.15) and (2.14)), we derive an equation for the separatrix:

$$\begin{aligned} P(p, e, \lambda) = & (e - 1)^2(e + 1)^3(-p + 6 + 2e) \\ & + \lambda p^3(e^3 - 5e^2 - 5e + 4p - 15) + \mathcal{O}(\lambda^2) = 0 \end{aligned} \quad (2.26)$$

which reduces to the usual Schwarzschild separatrix  $p = 6 + 2e$  at  $\lambda = 0$ . We see in Figure 2 the evolution of the separatrix from Schwarzschild to SdS both with a fixed  $\lambda$  in a 2D contour plot, and a continuous effect of  $\lambda$  in a 3D contour plot. The main effect of the cosmological constant is to eliminate most eccentric orbits and larger orbital sizes in the stable bound parameter space. This can be already seen in the energy and angular momentum, (equation (2.15) and (2.14)), wherein more eccentric and larger orbits are affected greater by the cosmological term, with the cosmological repulsion due to  $\lambda$  dominating making the orbits unbound. The maximum  $\lambda$  for bound orbits to occur is  $\lambda = 4/16875 \sim 2.37 \times 10^{-4}$  at  $(p = 7.5, e = 0)$  which produces a single stable bound orbit  $(p = 7.5, e = 0, \lambda = 4/16875)$ .

We can solve for the real roots in  $p$  of equation (2.26) perturbatively using the method of dominant balance [69] and see that there are two relevant curves,

$$p_{\text{inner,pl}} = 6 + 2e + \lambda \frac{8(3 - e)^2(3 + e)^3}{(1 - e^2)^2} + \mathcal{O}(\lambda^2) \quad (2.27)$$

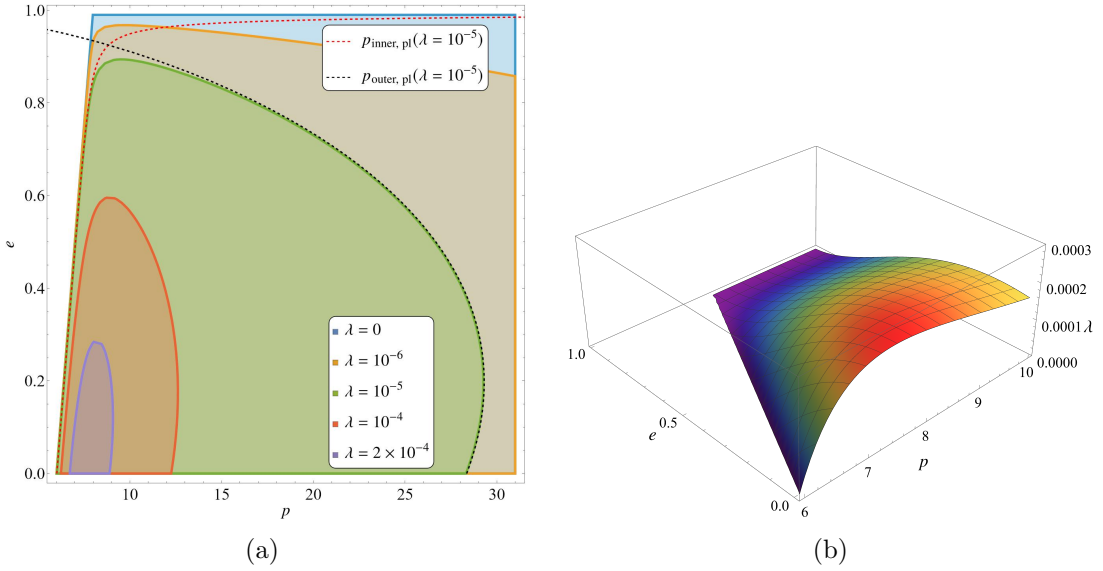


**Figure 2:** The separatrix equation  $P(p, e, \lambda)$  (equation (2.26)) in  $(p, e)$  space. In (a) the contours have varying  $\lambda$  with the filled region as the allowable parameter space for stable bound orbits. Introducing a  $\lambda > 0$  makes most eccentric orbits unbound. We see in the red and violet curve that a sufficiently high cosmological constant would also make orbits with high separation (larger orbits) also unbound. In (b) we show a continuous variation of  $\lambda$  onto the phase space  $(p, e)$  wherein the marginally bound orbits are the points lying on the surface.

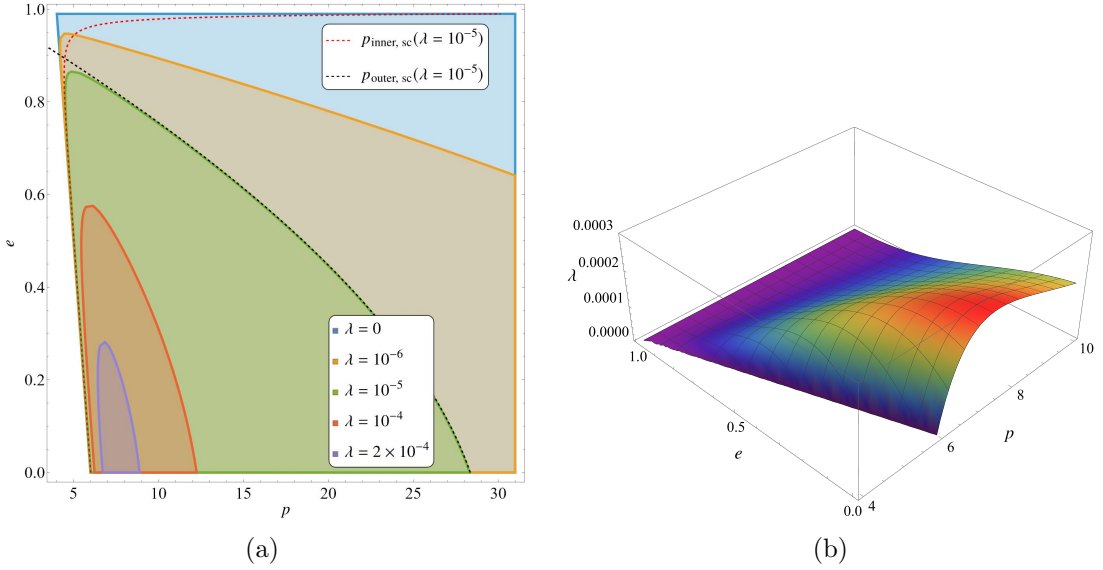


**Figure 3:** Similar contour plot and 3D plot to Figure 2 but with the scattering separatrix equation  $S(p, e, \lambda)$  (equation (2.30)).

and

$$p_{\text{outer,pl}} = -\frac{1}{12}(e-3)^2(e+1) + \left(\frac{(e-1)^2(e+1)^3}{4\lambda}\right)^{1/3} + \mathcal{O}(\lambda^{1/3}). \quad (2.28)$$

The two curves (equations (2.26) and (2.28)) form approximately the boundary of the region of bound orbital parameters, one as an “inner” separatrix, and one as an “outer” separatrix. The main observation here is the coupling of the cosmological constant with eccentricity, producing a tighter constraint for allowable orbits of higher eccentricity.

Both separatrices, equations (2.27) and (2.28), are also placed in Figure 1a and 1b to see how they limit the constant curves of  $(E, L)$  and  $(p, e)$ . This boundary extends to very large  $p$  for small enough  $\lambda$  but for a nontrivial  $\lambda$ , we see here a distinct feature of the SdS spacetime. The separatrices may imply that the presence of the cosmological constant limits the existence of very large orbits, making them unstable since the dynamics due to the cosmological repulsion dominates the opposing central gravitational attraction of the black hole. We further check this claim in the next part by examining the nature of marginally bound orbits associated with an outer unstable extrema.

### 2.3.2 Scattering separatrix

The earlier analysis only applies on marginally bound orbits in relation to the inner unstable extrema, wherein we have analyzed the region of bound orbits merging with the plunge region. This amounts to solving for the extrema with the radial distance evaluated at the periapsis. We can now examine the locus of parameters that merges the apoapsis to the outer unstable extrema by examining:

$$\frac{dV_{\text{eff}}}{dr}\Big|_{r=r_a} = 0 \quad (2.29)$$

which produces a distinct separatrix polynomial obtained earlier:

$$S(p, e, \lambda) = (e-1)^3(e+1)^2(2e+p-6) - \lambda p^3(e^3+5e^2-5e-4p+15) + \mathcal{O}(\lambda^2) = 0. \quad (2.30)$$

The contours of  $\lambda$  satisfying  $S(p, e, \lambda)$  is distinct from the separatrix polynomial,  $P(p, e, \lambda)$ , (equation (2.26)), and can be seen in Figure 3. We call  $P(p, e, \lambda)$  as the plunge separatrix since orbits outside the region it bounds will plunge to the black hole while we call  $S(p, e, \lambda)$  as the scattering separatrix since orbits outside the region it bounds will scatter to the cosmological horizon. The scattering separatrix also has maximum parameters  $\lambda = 4/16875 \sim 2.37 \times 10^{-4}$  at  $(p = 7.5, e = 0)$  equivalent to the parameters derived from the limits of the plunging separatrix. When solved for  $p$  using a dominant balance method, we also obtain two real physical solutions in  $p$  distinct from equation (2.27) and (2.28),

$$p_{\text{inner,sc}} = 2(3-e) - \frac{8(e+3)^2(e-3)^3\lambda}{(e^2-1)^2} + \mathcal{O}(\lambda^2), \quad (2.31)$$

$$p_{\text{outer,sc}} = \frac{1}{12}(3+e)^2(1+e) + \left(\frac{(1-e)^3(1+e)^2}{4\lambda}\right)^{1/3} + \mathcal{O}(\lambda^{1/3}). \quad (2.32)$$

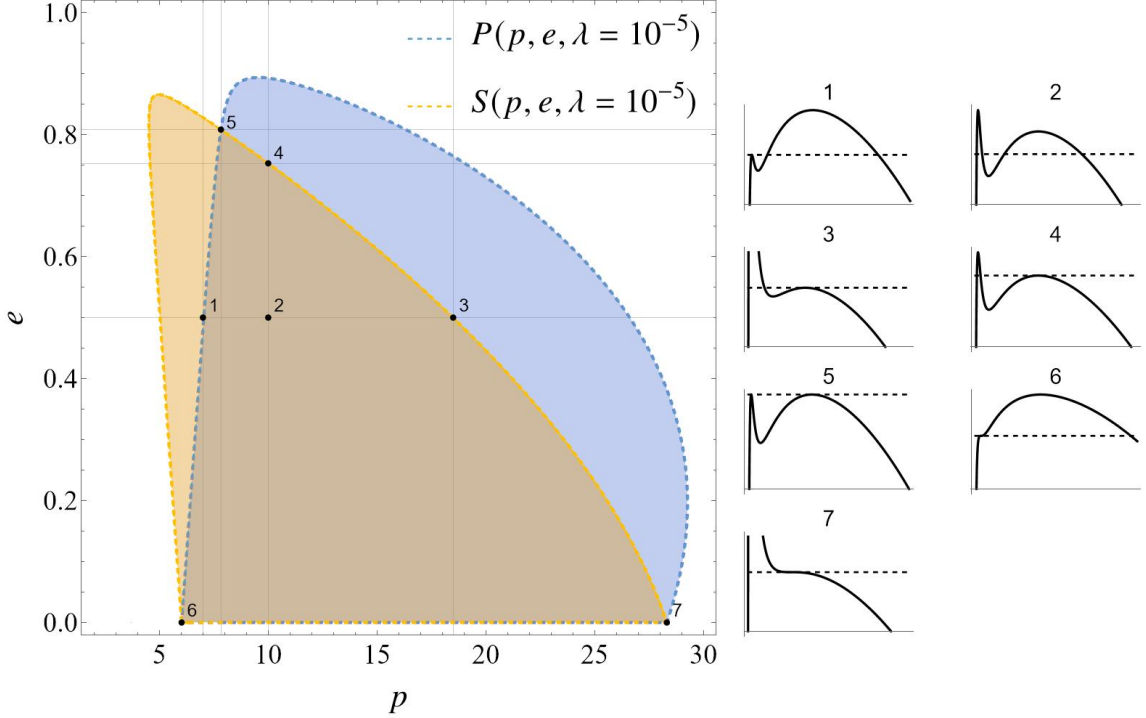


**Figure 4:** Potential shapes,  $V(r)$  vs  $r$ , (black curves in the right with dashed line as the orbital energy,  $E$ ) of selected orbital parameters (black dots) in  $(p, e)$  space. The intersection of orange and blue region contains the space of all bound orbits. The orange boundary (orange dashed line) marks the point at which orbits are marginally bound and may scatter away to the cosmological horizon while the blue boundary (blue dashed line) marks the points at which orbits are also marginally bound but may plunge to the black hole. The complement of the colored regions are unbound and may either plunge or scatter away.

This solution marks the boundary at which orbits will stay bounded and not scatter away as opposed to equation (2.28) which is the curve that marks the boundary at which orbits will stay bounded and not plunge to the black hole. We can now establish a hierarchy of lengthscales where our perturbative solutions will be valid, by examining the colored regions in Figure 4. We impose the hierarchy of the following appropriate lengthscales as:

$$p_h < p_{\text{inner,pl}} < p < p_{\text{outer,sc}} \ll p_c \quad (2.33)$$

with  $p_h = 2 + 8\lambda$ ,  $p_c = \lambda^{-1/2} - 1$  as the position of the black hole and cosmological horizon in  $(p, e)$  space. Stable bound orbits occur in the region,  $p_{\text{inner,pl}} < p_{\text{stable}} < p_{\text{outer,sc}}$ . An interesting feature in the region of bound orbits is the intersection between the plunging and scattering separatrix (equation (2.26) and (2.30)) that can be seen in Figure 4. The points of intersection (Point 5 in Figure 4) are marginally bound orbits and can either plunge or scatter away, depending on what direction  $p$  or  $e$  is changed by a small perturbation. These points are located in the parameter space at i.)  $(p = \frac{1}{2}(e^2 + 15), e = 1 - 8\lambda^{1/3})$ , at ii.) the innermost stable circular orbit (ISCO) and iii.) at the outermost stable circular orbit (OSCO).

The shifted ISCO can now be obtained by examining the circular limit,  $e \rightarrow 0$ , of the separatrix equation (equation (2.27)). This transforms the separatrix to  $(p - 6)(1836\lambda - 1) +$

$1944\lambda = 0$ , leading to the shifted ISCO,

$$p_{\text{ISCO}}(\lambda) = r_{\text{ISCO}}(\lambda) = 6 + 1944\lambda + \mathcal{O}(\lambda^2). \quad (2.34)$$

This means that a compact object orbiting circularly a  $M = 10^6 M_\odot$  SMBH under a  $\lambda = 10^{-6}$  de Sitter spacetime are unstable and might plunge at an additional distance of  $p < \mathcal{O}(10^3)$  km from the black hole. For a realistic  $\Lambda = 10^{-50}$  the additional distance of plunge is  $10^{-29}$  km for circular orbits, but could reach as high as  $10^{-26}$  km for highly eccentric orbits of  $e = 0.99$ . This is a negligible effect for a realistic cosmological constant value. We also derive an outermost stable circular orbit (OSCO),  $p_{\text{OSCO}}$  from equation (2.28) by setting  $e \rightarrow 0$ , leading to:

$$p_{\text{OSCO}}(\lambda) = r_{\text{OSCO}}(\lambda) = \left(\frac{1}{4\lambda}\right)^{1/3} - \frac{3}{4} + \mathcal{O}(\lambda^{1/3}). \quad (2.35)$$

As an example, for a  $M = 10^6 M_\odot$  SMBH under a  $\lambda = 10^{-6}$  SdS spacetime, circular orbits are restricted to the region  $p < 10^6$  km and for a more realistic value of  $\Lambda = 10^{-50}$  km $^{-2}$  the bound gets pushed to  $p < 10^{15}$  km.

Going back to the orbital energy and angular momentum at the separatrix, we examine the effect of the cosmological constant on the minimum and maximum values these quantities can hold. We evaluate the energy and the angular momentum at the approximate plunging separatrix equation (equation (2.27)):

$$E^2|_{\text{pl}} = \frac{8}{9-e^2} - \lambda \frac{32(e+3)(3e^2-2e+3)}{(3-e)(e^2-1)^2} \quad (2.36)$$

$$L^2|_{\text{pl}} = \frac{4(e+3)^2}{(3-e)(e+1)} + \lambda \frac{32(e+3)^4(e^3-5e^2-e-3)}{(3-e)(1-e)^2(e+1)^4} \quad (2.37)$$

which evaluates at  $E^2 > \frac{8}{9} - 24\lambda$  and  $L^2 > 12 - 2592\lambda$  for circular orbits. For eccentric orbits, neglecting high eccentricities of order  $\mathcal{O}((1-e)^{-1})$ , we have  $E^2 < 16 - 768\lambda$  and  $L^2 < 4 - 48\lambda$ . As expected from earlier results, the energy and angular momentum at the separatrix is decreased by a factor due to the cosmological constant. This would mean that lower energy and angular momentum would be required for orbits to plunge the black hole due to the expansion of spacetime, taking it longer to inspiral if we naively assume equal rates of energy and angular momentum loss for particles in a Schwarzschild and SdS spacetime.

### 3 Adiabatic orbital evolution

As the compact object inspirals toward the black hole, it emits gravitational radiation, which carries away energy and angular momentum from its motion. In the leading post-Newtonian (pN) approximation, the quadrupolar formula for the secularly averaged energy and angular momentum flux measured at the cosmological horizon, has been studied extensively by Bonga among others [32, 33, 45]. For sources inside asymptotically flat spacetimes, the gravitational radiation is defined at the “far-away wave zone” using a  $1/r$  expansion and then performing a temporal average over the orbital period. For asymptotically - de Sitter ( $\Lambda > 0$ ) spacetimes, the technique used by Bonga and Ashtekar [40, 41] was to define the radiative modes in the future null infinity ( $\mathcal{I}^+$ ) using a late-time expansion replacing the expansion in  $1/r$ . In

particular, the radiation field was defined to be the following:

$$\mathcal{Q}_{ij} := \left( \mathcal{L}_T^3 Q_{ij}^{(\rho)} + 3H\mathcal{L}_T^2 Q_{ij}^{(\rho)} + 2H^2 \mathcal{L}_T Q_{ij}^{(\rho)} + H\mathcal{L}_T^2 Q_{ij}^{(p)} + 3H^2 \mathcal{L}_T Q_{ij}^{(p)} + 2H^3 Q_{ij}^{(p)} \right) \Big|_{t \rightarrow t_{\text{ret}}} \quad (3.1)$$

with  $H = (\frac{\Lambda}{3})^{1/2}$ ,  $\mathcal{L}_T$  is the Lie derivative along the de Sitter time translational Killing vector and is related to the coordinate time  $t$  by  $\mathcal{L}_T = \partial_t - 2(\frac{\Lambda}{3})^{1/2}$ . The energy of the gravitational radiation at  $\mathcal{I}^+$  is defined to be the conserved current associated with a modified time-translation vector field. The averaged fluxes of energy and angular momentum radiated through  $\mathcal{I}^+$  of a compact source was derived [70] to be the integral of the mass ( $\rho$ ) and pressure ( $p$ ) quadrupole moments  $\mathcal{Q}_{ij} = \partial_t^3 Q_{ij}^{(\rho)} - (3\Lambda)^{1/2} \partial_t^2 Q_{ij}^{(\rho)} + \frac{2}{3}\Lambda \partial_t Q_{ij}^{(\rho)} + (\frac{\Lambda}{3})^{1/2} \partial_t^2 Q_{ij}^{(p)} - \frac{\Lambda}{3} \partial_t Q_{ij}^{(p)}$ ,

$$\begin{aligned} \langle \mathcal{P} \rangle &= \frac{G}{5} \langle \mathcal{Q}_{ij} \mathcal{Q}_{ij} - \frac{1}{3} \mathcal{Q}^2 \rangle \\ \langle \dot{L}_k \rangle &= \frac{2G}{5} \epsilon_{ikm} \left\langle \mathcal{Q}_{ij} \left( \mathcal{L}_T^2 Q_{ij}^{(\rho)} + \left( \frac{\Lambda}{3} \right)^{1/2} (\mathcal{L}_T Q_{ij}^{(\rho)} + \mathcal{L}_T Q_{ij}^{(p)}) + \frac{\Lambda}{3} Q_{ij}^{(p)} \right) \right\rangle \end{aligned} \quad (3.2)$$

evaluated at the retarded time  $t_{\text{ret}} = -(\frac{\Lambda}{3})^{-1/2} \ln \left( (\frac{\Lambda}{3})^{1/2} (r - \eta) \right)$  with  $\eta$  as the de Sitter conformal time. We reexpress the fluxes in terms of the orbital parameters  $(p, e)$  noting that we also neglect the pressure quadrupole moment in the leading order,

$$\begin{aligned} \frac{dE}{dt} &= -\frac{32}{5} \frac{1}{p^5} \left( 1 + \frac{73}{24} e^2 + \frac{37}{96} e^4 \right) (1 - e^2)^{3/2} \\ &\quad - \lambda \frac{8}{3p^2} \left( 4 - (1 - e^2)^{1/2} \right) (1 - e^2)^{3/2} + \mathcal{O}(\lambda^2) \end{aligned} \quad (3.3)$$

$$\begin{aligned} \frac{dL}{dt} &= -\frac{32}{5} \frac{1}{p^{7/2}} \left( 1 + \frac{7}{8} e^2 \right) (1 - e^2)^{3/2} \\ &\quad - \lambda \frac{8}{p^{1/2}} (1 - e^2) + \mathcal{O}(\lambda^2). \end{aligned} \quad (3.4)$$

It is important to note that these expressions are valid only within the the range specified by equation (2.33). Under the conditions described by equation (2.33), for  $p = p_{\text{stable}}$ , the flux contribution from the cosmological constant remains subdominant compared to the Peters-Mathews fluxes. However, this contribution becomes comparable in magnitude only for  $p > p_{\text{stable}}$ , corresponding to unbound orbits.

The expressions above (equations (3.3) and (3.4)) indicate that a nonzero energy and angular momentum flux implies the energy and angular momentum of a bound orbit must change over time, although implicitly through the orbital parameters,

$$(L, E) \rightarrow (L(p(t), e(t)), E(p(t), e(t))). \quad (3.5)$$

The flux of energy and angular momentum will cause the orbital trajectory to evolve continuously, resulting in a dynamic orbit characterized by time-dependent orbital parameters. Given that we have defined the bound orbits as ellipses (equation (2.10)), long-term secular

changes [71] in the orbital parameters will manifest as an evolving ellipse, or an osculating orbit.

We now outline the derivation for the orbital evolution equations. To begin, we observe that the time derivatives of energy and angular momentum can be directly related to time derivatives of the orbital elements,

$$\frac{dE}{dt} = \frac{\partial E}{\partial p} \frac{dp}{dt} + \frac{\partial E}{\partial e} \frac{de}{dt}, \quad \frac{dL}{dt} = \frac{\partial L}{\partial p} \frac{dp}{dt} + \frac{\partial L}{\partial e} \frac{de}{dt}. \quad (3.6)$$

We utilize the Jacobian  $J_{ij} = \partial_i \rho_j$  where  $i$  corresponds to the elements of  $(p, e)$  and  $\rho_j$  represents the elements of  $(L, E)$ . The evolution of the orbital parameters can then be expressed as:

$$\begin{pmatrix} \frac{dp}{dt} \\ \frac{de}{dt} \end{pmatrix} = (J_{ij})^{-1} \begin{pmatrix} \frac{dL}{dt} \\ \frac{dE}{dt} \end{pmatrix}. \quad (3.7)$$

In this derivation, circular orbits,  $e = 0$  are excluded, as they render  $J_{ij}^{-1}$  singular as discussed in Section 2.2. The evolution of circular orbits will instead be addressed separately in the next subsection, Section 3.1.

Using the fluxes (equations (3.3) and (3.4)) and the derivatives of the corrected energy and angular momentum (equations (2.16) and (2.17)), the orbital evolution equations given by:

$$\begin{aligned} \dot{p}(p, e) &= 2\sqrt{p} \dot{E}_N \\ &- \lambda \left[ 2\sqrt{p} \dot{E}_\lambda + \epsilon \frac{3p^{7/2}}{(e^2 - 1)^2} \dot{L}_N - \epsilon \frac{4p^5}{(e^2 - 1)^3} \dot{E}_N \right] + \mathcal{O}(\lambda^2) \end{aligned} \quad (3.8)$$

$$\begin{aligned} \dot{e}(p, e) &= \frac{p}{e} \dot{L}_N + \frac{(e^2 - 1)}{\sqrt{p}e} \dot{E}_N \\ &- \frac{\lambda}{e} \left[ p \dot{L}_\lambda + \frac{(e^2 - 1)}{\sqrt{p}} \dot{E}_\lambda + \epsilon \frac{7p^{5/2}}{2(e^2 - 1)} \dot{L}_N - \epsilon \frac{4(e^2 + 1)p^4}{(e^2 - 1)^3} \dot{E}_N \right] + \mathcal{O}(\lambda^2). \end{aligned} \quad (3.9)$$

The orbital evolution equations involve de Sitter terms of order  $\epsilon (= 1)$ , a fiducial parameter, to highlight the effect of the corrected conserved energy,  $E = E_N + \epsilon \lambda E_\lambda$ , and angular momentum,  $L = L_N + \epsilon \lambda L_\lambda$  (equations (2.15) and (2.14)). These orbital evolution equations represent the correct form of the orbital dynamics up to leading  $\mathcal{O}(\lambda)$  and leading  $p$  - dependence. Notably, the earlier work by Hoque and Aggarwal [33] did not account these linear  $\lambda$  terms, which should also contribute to the evolution of the orbital parameters.

We further observe that the orbital evolution equations are only valid within the eccentricity range  $0 < e < 1$ , evidenced by the  $e^{-1}$  divergence for  $e = 0$  orbits. In standard literature, the  $e^{-1}$  divergence is typically removed by using the Peters-Mathews fluxes or by incorporating modified fluxes due to the cosmological constant, as discussed in [33]. It will be evident later in this section that the new terms due to the modified energy and angular momentum retain this divergence in eccentricity.

The gravitational fluxes (equations (3.3) and (3.4)) are valid only in the weak-field regime as noted earlier. Therefore, we now present the form of the orbital evolution equations for bound orbits far from the black hole, using a large  $p$  expansion for the equations under the relation (2.33). The resulting secular evolution equations  $\dot{p}$  and  $\dot{e}$  are given by:

$$\begin{aligned}\dot{p}(p, e) = & -\frac{64}{5}p^{-3}(1-e^2)^{3/2}\left(1+\frac{7}{8}e^2\right) \\ & -\lambda\left[16(1-e^2)-\epsilon\frac{4(26e^4-283e^2-168)}{15(1-e^2)^{3/2}}+\mathcal{O}(\lambda p)\right]\end{aligned}\quad (3.10)$$

$$\begin{aligned}\dot{e}(p, e) = & -\frac{304}{15}p^{-4}e(1-e^2)^{3/2}\left(1+\frac{121}{304}e^2\right) \\ & -\lambda\left[\frac{32}{3}p^{-1}e^{-1}(1-e^2)^{3/2}\left(1-(1-e^2)^{1/2}\right)\right. \\ & \left.-\epsilon p^{-1}e^{-1}\frac{2(73e^6-784e^4-965e^2-24)}{15(1-e^2)^{3/2}}+\mathcal{O}(\lambda p^{-2})\right].\end{aligned}\quad (3.11)$$

Equations (3.10) and (3.11) reduce to the post-Newtonian (2.5 pN) orbital evolution equations when  $\lambda = 0$  [72], but with the  $p$  dependence replacing the semi-major axis  $a$ . In the following subsections, we will demonstrate how initially circular and eccentric orbits evolve using these equations.

### 3.1 Evolution of circular orbits

Earlier work [33, 72] has shown that the circular limit of the orbital equations ((3.10) and (3.11)) is regular at the  $e \rightarrow 0$  limit, implying that circular orbits will remain circular due to the vanishing of  $\dot{e}$ . However, the circular limit of the eccentricity evolution equation (equation (3.11)) is ill-defined, as the terms contributed by the cosmological constant do not eliminate the  $e^{-1}$  divergence present in equation (3.9). Therefore, we must develop an independent method to analyze how circular orbits will evolve under release of gravitational fluxes.

One approach to understanding how circular orbits evolve is to shift the analysis to  $(E, L)$  space (visualized in Fig. 1a) and examine how the fluxes  $(\dot{E}, \dot{L})$  influence the space of circular orbits, represented by the  $e = 0$  curve. The tangents,  $dE/dL$ , lying in the  $e = 0$  curve correspond to the rates of energy and angular momentum change that will make an initially circular orbit circular. If the tangents stay close and trace the  $e = 0$  curve, this would indicate that the fluxes of energy and angular momentum necessarily maintain the circularity of the orbit. However, if the tangents deviate away from the  $e = 0$  curve, it would suggest that circular orbits will lose its circularity due to the fluxes. For the Peters-Mathews fluxes, this can be easily demonstrated by first taking the  $\lambda = 0$  limit, followed by the  $e = 0$  limit of the fluxes (equations (3.3) and (3.4)),

$$\left.\frac{dE}{dL}\right|_{\text{flux, } \lambda=0} = \frac{dE}{dt} \left(\frac{dL}{dt}\right)^{-1} = \frac{p^{-5}}{p^{-7/2}} = p^{-3/2}. \quad (3.12)$$

,  $e=0$  In the conservative case, the energy and angular momentum in terms of  $(p, e)$  (equations (2.17) and (2.16)), yield the ratio of energy and angular momentum as

$$\left.\frac{dE}{dL}\right|_{\text{circ, } \lambda=0} = \frac{dE}{dp} \left(\frac{dL}{dp}\right)^{-1} = \frac{p^{-2}}{p^{-1/2}} = p^{-3/2}. \quad (3.13)$$

The flux ratio (equation (3.12)) match the rates at which a circular orbit remains circular (equation (3.13)), indicating that under the Peters-Mathews fluxes, circular orbits will indeed remain circular until plunge.

Repeating the analysis with the inclusion of the cosmological constant  $\lambda$ , we see that the flux ratio take the form:

$$\frac{dE}{dL} \bigg|_{\text{flux, } \lambda \neq 0, p=\tilde{p}} = \frac{\sqrt{\lambda}}{\tilde{p}^{3/2}} + \mathcal{O}(\lambda \tilde{p}^{3/2}), \quad (3.14)$$

for the intermediate scale  $\tilde{p} = p\lambda^{1/3} \ll 1$ , which satisfies the condition for stable orbital parameters from equation (2.33). On the other hand, the tangents to the SdS  $e = 0$  curve follow the form:

$$\frac{dE}{dL} \bigg|_{\text{circ, } \lambda \neq 0, p=\tilde{p}} = \frac{\sqrt{\lambda}}{\tilde{p}^{3/2}} - \frac{1}{2}\sqrt{\lambda}\tilde{p}^{3/2} + \mathcal{O}(\lambda \tilde{p}^{5/2}). \quad (3.15)$$

Comparing equations (3.14) and (3.15), we see an additional term in the expression for the tangents, unlike the match between equations (3.12) and (3.13). This indicates that the SdS fluxes drives the orbits away from the  $e = 0$  curve, causing initially circular orbits to break their circularity. As  $\lambda \rightarrow 0$ , the SdS flux ratio reduce (equation (3.14)) to Peters-Mathews flux ratio (equation (3.12)) and the Schwarzschild  $e = 0$  tangents (equation (3.13)) become,

$$\frac{dE}{dL} \bigg|_{\text{flux, } \lambda \rightarrow 0} = \frac{dE}{dL} \bigg|_{\text{circ, } \lambda=0} = p^{-3/2}. \quad (3.16)$$

Thus for  $\lambda \rightarrow 0$ , a Newtonian orbit will remain circular. This result was also demonstrated by [33] using the orbital evolution equations rather than the rates of energy and angular momentum change. However, a key point of this paper is that the energy and angular momentum of a bound orbit will be influenced by the cosmological constant, which means that a Newtonian description of a bound orbit will be inaccurate.

The tangents to the  $e = 0$  curve (equation (3.15)) indicate that inside the region where  $p \ll \lambda^{-1/3}$  or at  $\tilde{p} \ll 1$ , the cosmological term is small and gravitational fluxes will indeed drive circular orbits to remain circular up to the leading order  $\mathcal{O}(\tilde{p}^{-3/2})$ . Closer to the outer separatrix,  $posco - p \ll 1$ , far from the intermediate scale  $\tilde{p}$ , the flux ratio becomes:

$$\frac{dE}{dL} \bigg|_{\text{flux, } p \rightarrow posco} = \frac{1}{p_{\text{OSCO}}^{3/2}} + \frac{3}{2p_{\text{OSCO}}^{5/2}} (posco - p) + \mathcal{O}((posco - p)^2) \quad (3.17)$$

which reduces, in the leading order in  $p$ , to the Peters-Mathews fluxes for  $\lambda \rightarrow 0$  or  $posco \rightarrow \infty$  (where the OSCO extends to infinity in the Schwarzschild spacetime). The tangents to the SdS  $e = 0$  curve near  $posco$  are given by (factoring out the flux (3.17) for easy comparison):

$$\frac{dE}{dL} \bigg|_{\text{circ, } p \rightarrow posco} = \frac{dE}{dL} \bigg|_{\text{flux}} \left( 1 - \lambda \frac{p_{\text{OSCO}}^3}{2} \right) + \mathcal{O}(\lambda (posco - p)^2). \quad (3.18)$$

Comparing the flux ratio and the  $e = 0$  tangents near the OSCO (equations (3.17) and (3.18)), we see that an additional term proportional to  $\lambda$  and  $posco$ . This means that in these

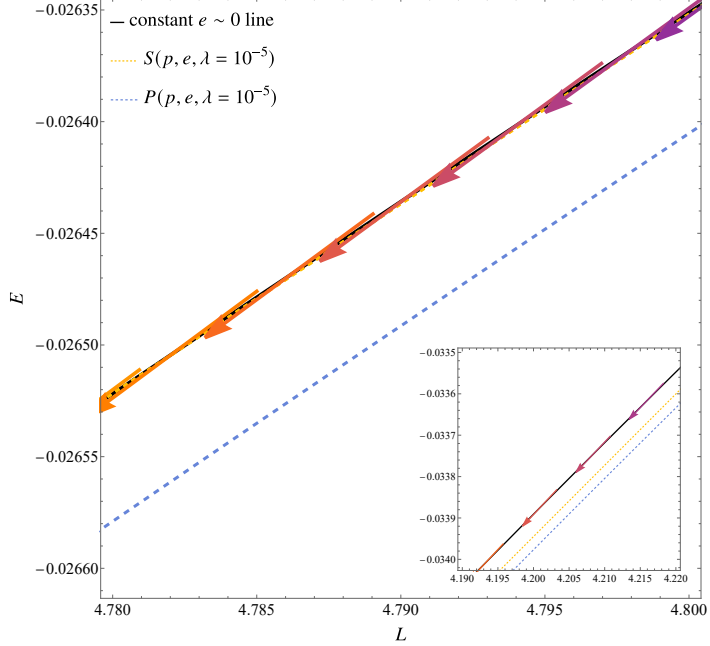


**Figure 5:** Gravitational flux (vectors) tangent to the  $e = 0$  curve (black) in the  $(E, L)$  space. We see here as discussed in Section 3.1 that far from the OSCO (inset, low  $(E, L)$ ), circularity is maintained (vectors lie along the black curve) but as for orbits with separation near the OSCO, the orbits will cross the scattering separatrix (yellow) and become unbound with the vectors crossing the yellow dashed line.

regions, gravitational fluxes will not preserve the circularity of the orbit. Thus in the region where  $(\text{posco} - p) \ll 1$ , near the outer separatrix, the SdS gravitational fluxes will not be sufficient to maintain the circularity of the orbital evolution.

As illustrated in Figure 5, at higher orbital separations, closer to the OSCO, gravitational fluxes will push the orbits outside the scattering separatrix (equation (2.30)) making the orbits unbound. In the inset of Figure 5, we see that for orbits far from the OSCO, (with low energy and angular momentum), gravitational fluxes will drive the orbits along the  $e = 0$  curve, maintaining their circularity.

### 3.2 Evolution of eccentric orbits

We now analyze equations (3.10) and (3.11) to understand the evolution of eccentric orbits. By examining the signs of the terms, we observe that the de Sitter contributions generally increase the magnitude of orbital parameter evolution. At first glance, the de Sitter terms seems to enhance the rate at which orbits shrink, leading to a faster inspiral and circularization. However, the second de Sitter term introduces a positive contribution, which counteracts this effect by decreasing the rate of inspiral and circularization. The competing influence highlights the complexity of the de Sitter modifications in the orbital evolution.

A particularly interesting feature emerges in the dependence of the de Sitter terms on the orbital parameters. Specifically, in the eccentricity evolution equation, the second de Sitter term exhibits an  $e^{-1}$  scaling, which diverges for very nearly circular orbits ( $e \rightarrow 0$ ). This is a novel effect introduced by the presence brought of the cosmological constant, affecting the late-time behavior of eccentricity evolution. In the regime where the second de Sitter

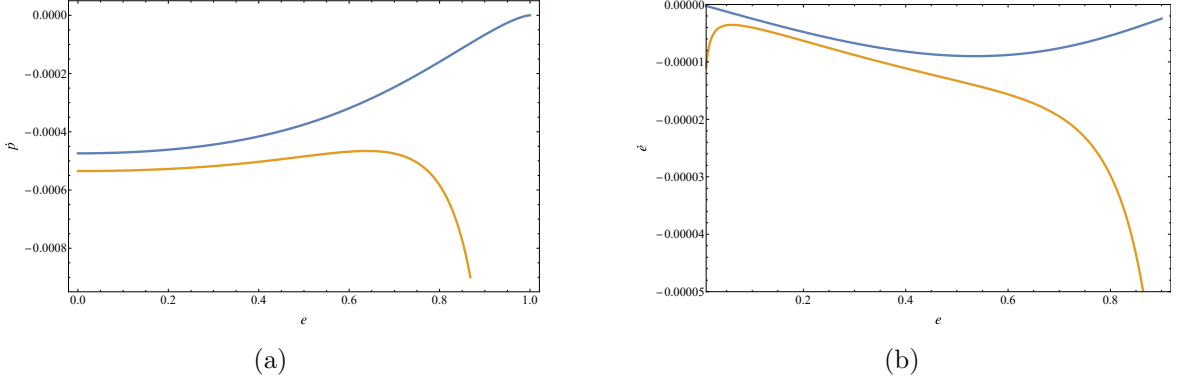


**Figure 6:** Dependence of orbital evolution,  $\dot{p}$  and  $\dot{e}$ , on eccentricity,  $e$ . Fixing the semi-latus at  $p = 30$  and cosmological constant  $\lambda = 10^{-6}$  for the SdS (yellow) case and  $\lambda = 0$  for the Schwarzschild case (blue), we show the rate of orbital parameter evolution with respect to eccentricity. We show in (a) the evolution of  $p$  as steadily decreasing reaching a constant maximum at the circular limit. We show in (b) the evolution of  $e$  is large for highly eccentric orbits and  $e \rightarrow 0$  orbits. The cosmological constant amplifies the decay of the orbital parameters continuously increasing at the low  $e$  region where the evolution in  $e$  is dominated by the de Sitter term.

term dominates, the eccentricity changes more rapidly than expected. Figure 6 illustrates the dependence of the orbital evolution equations on eccentricity, further demonstrating these effects.

The divergence in the low-eccentricity regime can be observed in equation (3.9) and can be attributed to a specific contribution of the cosmological constant to the eccentricity evolution, this contribution is given by:

$$\frac{de}{dt} \Big|_{e \rightarrow 0} = \epsilon \frac{\frac{\partial L_\lambda}{\partial p}}{\frac{\partial L_N}{\partial p}} \dot{E} \left( \frac{\partial E_N}{\partial e} \right)^{-1} - \epsilon \frac{\frac{\partial E_\lambda}{\partial p}}{\frac{\partial L_N}{\partial p}} \dot{L} \left( \frac{\partial E_N}{\partial e} \right)^{-1} \sim e^{-1}. \quad (3.19)$$

The derivative of the Keplerian energy with respect to  $e$  follows the scaling relation  $\frac{\partial E_N}{\partial e} \sim e$ . For small eccentricities  $e$ , this term becomes significantly smaller than the factors  $\frac{\partial L_\lambda}{\partial L_N} \dot{E} \sim 1$  and  $\frac{\partial E_\lambda}{\partial L_N} \dot{L} \sim 1$ . Furthermore, this effect persists because the relation  $\frac{\partial L_\lambda}{\partial p} \dot{E} < \frac{\partial E_\lambda}{\partial p} \dot{L}$  or  $\frac{\partial L_\lambda}{\partial L} < \frac{\partial E_\lambda}{\partial E}$  holds. As a result, the evolution of eccentricity is significantly accelerated in the low - eccentricity parameter space.

As discussed earlier in this section, initially eccentric orbits tend to decrease in eccentricity throughout their evolution. The decrease in eccentricity accelerates as the orbits approach circularity. For orbits far from the OSCO, circular orbits will remain circular, while eccentric orbits eventually circularize. From the previous subsection, it was shown that orbits close to the outer separatrix, near the outermost stable circular orbit (OSCO, equation (2.35)), the SdS gravitational fluxes fail to maintain the circularity of an initially circular SdS orbit. Such orbits will become unbound over time. Near the OSCO, where  $p_{\text{OSCO}} - p \ll 1$ , the

eccentricity evolution equation (equation (3.11)) takes the form:

$$\begin{aligned} \frac{de}{dt} \Big|_{p \rightarrow \text{posco}, e \ll 1} &\approx -\frac{304e}{15p_{\text{OSCO}}^4} - \frac{1216e(p_{\text{OSCO}} - p)}{15p_{\text{OSCO}}^5} + \lambda \frac{(-640e^2 p_{\text{OSCO}}^3 + 37407e^2 + 17064)}{120ep_{\text{OSCO}}^4} \\ &\quad + \mathcal{O}((p_{\text{OSCO}} - p)^2) + \mathcal{O}(\lambda(p_{\text{OSCO}} - p)). \end{aligned} \quad (3.20)$$

This equation vanishes when

$$\begin{aligned} p \Big|_{\dot{e}=0} &\approx \frac{5p_{\text{OSCO}}}{4} + \lambda \left( -\frac{2133p_{\text{OSCO}}}{1216e^2} + \frac{p_{\text{OSCO}}(640p_{\text{OSCO}}^3 - 37407)}{9728} \right) \\ &\quad + \mathcal{O}(\lambda e^2). \end{aligned} \quad (3.21)$$

The first term is a constant which exceeds  $p_{\text{OSCO}}$  by a fixed factor. Hence, for bound orbits with  $p < p_{\text{OSCO}}$ , the eccentricity evolution is always decreasing, reaching zero only if the initial semi-latus rectum is at  $p = 5p_{\text{OSCO}}/4$ , which lies outside the region of stable orbits. This implies that, within the bound region, eccentricity will always decrease. We summarize the eccentricity evolution of bound orbits as:

- *Far from the OSCO:*
  - Circular orbits will maintain circularity up to  $\mathcal{O}(\tilde{p}^{3/2})$ .
  - Eccentric orbits will gradually circularize.
- *Near the OSCO:*
  - Circular orbits will be pushed outside OSCO, becoming unbound.
  - Eccentric orbits near circularity will also be pushed outside OSCO, becoming unbound.

The orbital evolution is obtained by solving equations (3.10) and (3.11), treating them as a system of coupled, nonlinear, ordinary differential equations where the orbital parameters evolve in time,  $p(t)$  and  $e(t)$ . To gain insight into the system before solving explicitly, we analyze equations (3.10) and (3.11) by interpreting the right-hand side as a set of vector fields in the  $(p, e)$  phase space. This allows us to construct a phase portrait of the differential equations, as shown in Figure 7. Similar to Schwarzschild case, gravitational radiation reaction in SdS spacetime generally leads to  $(p, e)$  decay. The key quantity in determining the direction of orbital evolution in phase space is the slope  $de/dp$ . When the slopes are higher, the vectors are steeper, indicating that eccentricity decay dominates the evolution. Conversely, lower slopes correspond to flatter vectors indicating that the inspiral dominates the evolution.

### 3.3 Inspiral, circularization and orbital trajectory

Before solving the orbital equations (3.8) and (3.9) for the inspiral and circularization rate, we first obtain realistic estimates on their magnitudes. For a circular EMRI of mass  $\mu = 10M_{\odot}$

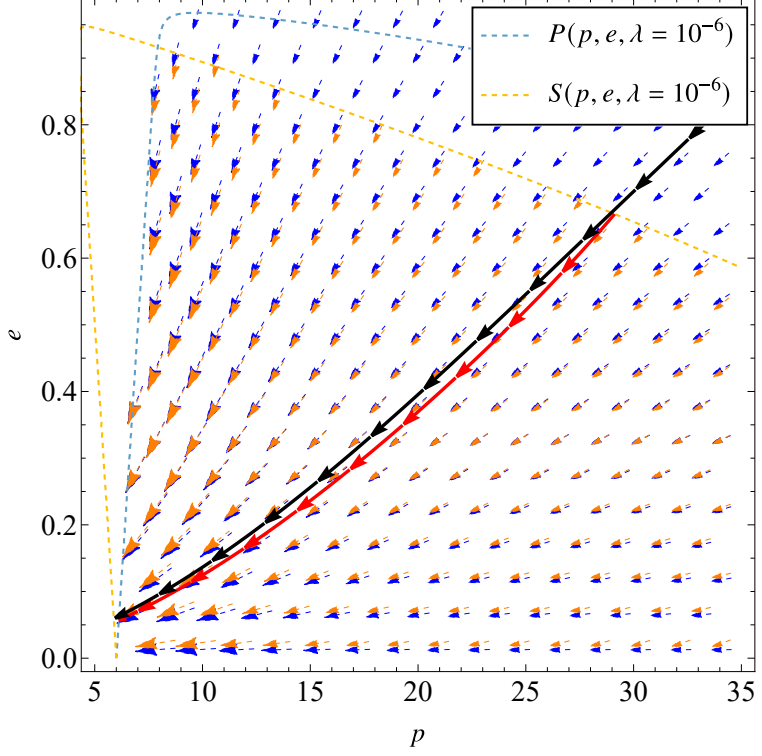


**Figure 7:** The flow of  $\dot{p}$  and  $\dot{e}$  in the phase plane  $(p, e)$  and the vector slope  $de/dp$  in Schwarzschild and SdS spacetime. In (a), we show the  $\dot{p}$  and  $\dot{e}$  as vectors following equations (3.10) and (3.11). Blue vectors denote orbital evolution in Schwarzschild spacetime ( $\lambda = 0$ ) while orange vectors are in Schwarzschild – de Sitter ( $\lambda = 10^{-6}$ ). Black vectors ( $\lambda = 0$ ) and red vectors ( $\lambda = 10^{-6}$ ) are fixed trajectories that meet at the same parameters,  $(p_0 = 30, e_0 = 0.7)$ . We see here that the black trajectory has a lower slope indicating slower eccentricity decay with respect to  $p$ . Sizes of the vectors indicate relative magnitudes.

orbiting a black hole of mass  $M = 10^6 M_\odot$  in a de Sitter universe of  $\Lambda \sim 10^{-50} \text{ km}^{-2}$ , the inspiral rate,  $\dot{p}$ , is estimated to be

$$\begin{aligned} \dot{p}(e_0 = 0) \sim & -10^{-12} \text{ km/yr} \left( \frac{1 \text{ pc}}{p_0} \right)^3 \left( \frac{M}{10^6 M_\odot} \right)^2 \left( \frac{\mu}{10 M_\odot} \right) \\ & -10^{-29} \text{ km/yr} \left( \frac{M}{10^6 M_\odot} \right) \left( \frac{\mu}{10 M_\odot} \right) \left( \frac{\Lambda}{10^{-50} \text{ km}^{-2}} \right). \end{aligned} \quad (3.22)$$

The estimate suggests that the de Sitter term becomes comparable to the leading term only when the EMRI is at an initial semi-latus rectum of  $p_{0,\text{insp}} \sim \mathcal{O}(10^6)$  pc. For eccentric inspirals, the inspiral rate follows the trend in Figure 6 that increases significantly at higher eccentricities, reducing  $p_{0,\text{insp}}$  for the de Sitter term to be comparable.

For circularization, we estimate the rate of eccentricity decay for an EMRI with an

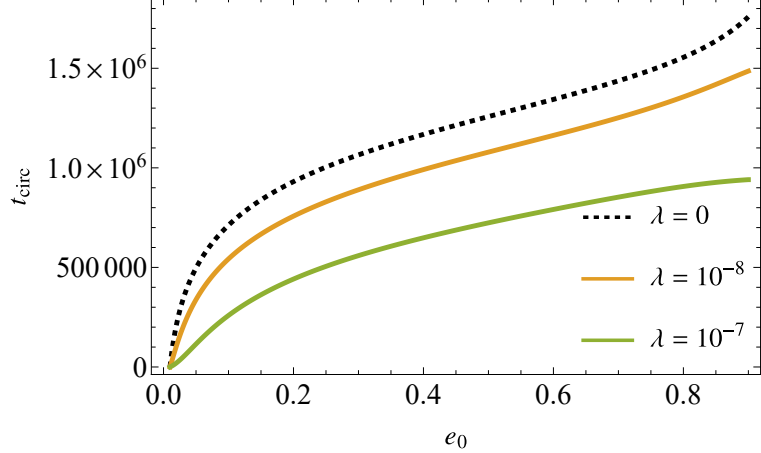


**Figure 8:** Numerical curves for  $t_{circ}$  for a fixed  $p = 50$  (with the assumption that it stays constant) and its dependence on  $e$  for varying  $\lambda$ . We see here that circularization time are reduced by the cosmological constant. As we increase the value of  $\lambda$ , highly eccentric orbits circularizes much faster.

initial eccentricity  $e = 0.7$ :

$$\begin{aligned} \dot{e} \Big|_{e_0=0.7} &\sim -10^{-26} \text{yr}^{-1} \left( \frac{1 \text{pc}}{p_0} \right)^4 \left( \frac{M}{10^6 M_\odot} \right)^2 \left( \frac{\mu}{10 M_\odot} \right) \\ &\quad - 10^{-42} \text{yr}^{-1} \left( \frac{1 \text{pc}}{p_0} \right) \left( \frac{M}{10^6 M_\odot} \right) \left( \frac{\mu}{10 M_\odot} \right) \left( \frac{\Lambda}{10^{-50} \text{km}^{-2}} \right). \end{aligned} \quad (3.23)$$

Similar to the inspiral rate, the de Sitter term becomes comparable to the leading decay term at distances  $p_{0,circ} \sim \mathcal{O}(10^5)$  pc. For lower eccentricities, the scaling follows the curve in Figure 6. The de Sitter term's influence on orbital evolution is only significant at distances well beyond the galactic scale. Moreover, since  $p_{0,insp} > p_{0,circ}$ , the effect of the cosmological constant on reducing the orbital size becomes noticeable before the effect on eccentricity decay. For a fixed orbital size, we can numerically integrate the equation for  $\dot{e}$  to estimate the circularization time and its dependence on  $e$  and  $\lambda$ . Specifically, we compute  $t_{circ} = t(e, p_{fixed}) = \int (de/dt)^{-1} de$ . Figure 8 shows the results for a fixed orbit size of  $p_{fixed} = 50$ . We observe that at a given value of cosmological constant, the circularization time is longest at high eccentricities. However, at larger values of  $\lambda$  the circularization time shortens at higher eccentricities.

To analyze the time evolution of the orbital parameters  $(p, e)$ , we numerically solve the system of ODE (equations (3.10) and (3.11)) for given initial configurations. The resulting solutions, illustrated in Figure 9, demonstrate that the presence of the cosmological constant is to increase the rate of orbital decay. As a consequence, the cosmological constant accelerates the inspiral of the CO, leading to an earlier plunge into the central BH.

We reconstruct hybrid orbital trajectories in the following manner. The method of osculating orbits [73, 74] supposes the true physical orbit evolves in time through its orbital parameters, such that at every instant, the orbit is a geodesic. The quasi-Keplerian equation of the orbit is of the form:

$$r(\psi) = \frac{pM}{1 + e \cos \psi} \rightarrow r(t) = \frac{p(t)M}{1 + e(t) \cos \psi(t)}. \quad (3.24)$$

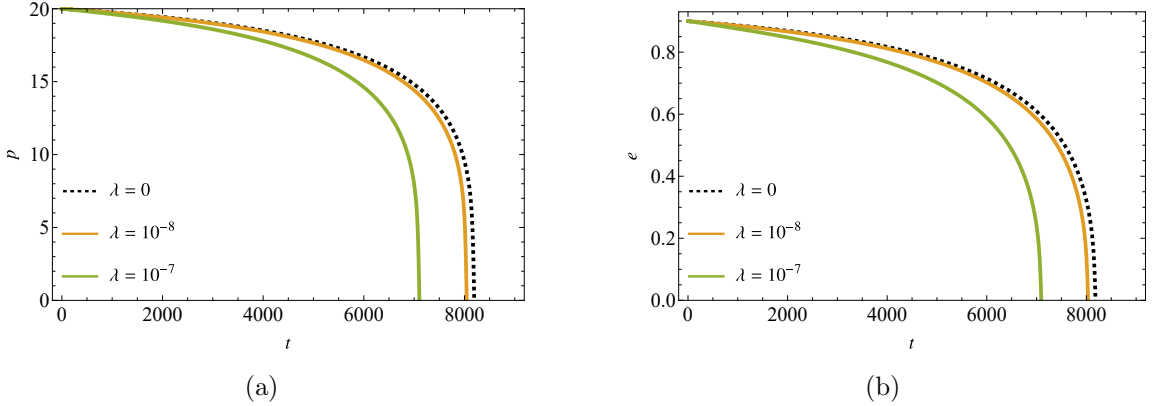


**Figure 9:** Numerical curves of  $p(t)$  and  $e(t)$  with initial parameters ( $p_0 = 20$ ,  $e_0 = 0.9$ ) for different cosmological constant values. We show here the general effect of the cosmological constant which is to reduce plunge and circularization times as the cosmological constant increases.

where the orbital parameters  $\{p, e, \psi\}$  are now functions of time.

The angular frequency,  $\omega$ , of the CO orbiting the central BH is derived directly from the geodesics of the SdS spacetime. Using the definition  $\omega = (d\phi/d\tau)(dt/d\tau)^{-1}$ , and considering the orbital plane at  $\theta = \pi/2$ , with the angular momentum  $L$  and energy  $E$  expressed in terms of  $(p, e)$  and  $r(\psi)$  for a bound orbit, the angular frequency in the large- $p$  limit is given by:

$$\omega = \left( \frac{L}{r^2} \right) \left( \frac{E}{f(r)} \right)^{-1} = n(1 + e \cos(\psi))^2 \quad (3.25)$$

where  $n$  is the corrected mean motion or the angular frequency of a circular orbit modified by the cosmological constant,

$$n = \frac{1}{p^{3/2}} - \lambda \left( \frac{p^{3/2}}{2} + \mathcal{O}(\lambda p^{1/2}) \right). \quad (3.26)$$

To eliminate oscillations in the angular frequency due to dependence on the true anomaly  $\psi$ , we perform an averaging procedure over a full orbital cycle.

$$\frac{1}{P} \int_{t_0}^{t_0+P} \omega dt = \frac{1}{P} \int_{t_0}^{t_0+P} n(1 + e \cos(\psi))^2 dt \quad (3.27)$$

Assuming that the argument  $\delta$  of the periapsis remains constant over one complete orbit,

$$\omega = \frac{d\phi}{dt} = \frac{d\psi}{dt} + \frac{d\delta}{dt} \sim \frac{d\psi}{dt}, \quad (3.28)$$

and we set  $dt = \omega^{-1} d\psi$ . Then we integrate:

$$\int_0^{2\pi} (1 + e \cos(\psi))^{-2} d\psi = \int_{t_0}^{t_0+P} n dt = \mathcal{M} = 2\pi \quad (3.29)$$

over  $\psi = (0, 2\pi)$  corresponding to the angle swept after a period  $P$  telling us that over a complete radial cycle, the orbit with angular frequency equal to the mean motion  $n$ , completes

a full cycle in  $\psi$ . Since the right hand side corresponds to the mean anomaly  $\mathcal{M}$ , which is equal to  $2\pi$ , the mean motion  $n$  serves as the averaged angular frequency over a single cycle from  $\psi = 0$  to  $\psi = 2\pi$  for a generic eccentric orbit. We consider the mean motion as the characteristic angular frequency of the orbit, which will directly govern the phase evolution of the emitted gravitational wave.

The osculating equations of the orbital parameters is appended by the equation for  $\psi$ ,

$$\frac{d\psi}{dt} = n(p)(1 + e \cos \psi)^2 \quad (3.30)$$

with  $n(p)$  (equation (3.26)) as the orbital mean motion as a function of  $p$ . Within a single cycle (an orbital period timescale), we impose that  $\psi$  only changes significantly, and that the changes in  $p$  and  $e$  happen only as a secular drift (adiabatic timescale, or the radiation reaction timescale). Within the adiabatic timescale, such that the true anomaly remains the single orbital parameter that changes within an orbital period, our hybrid orbital trajectory will be valid. Considering the radial motion along an orbital  $x - y$  plane, we have the positions:

$$x = r(t) \cos \phi(t), \quad y = r(t) \sin \phi(t) \quad (3.31)$$

with the coordinate azimuthal angle  $\phi = \psi + \delta$ , related to the angle at the periapsis, which also becomes an evolving parameter  $\delta \rightarrow \delta(t)$ . We only include the leading order (1pN) rate of change in  $\delta$ ,

$$\Delta\delta_{1pN} = \frac{6\pi}{p}. \quad (3.32)$$

Since  $\delta$  depends on the evolving orbital size, we can estimate how much it changes due to the contribution of the cosmological constant to the gravitational flux. Using the dimensionalized inspiral rate  $\dot{p}$  from (3.22), we find that after one complete orbit, the periapsis shifts by a coordinate angle:

$$\phi = 2\pi \left( 1 + \frac{3}{p} \frac{GM}{c^2} \right) \sim 2\pi \left( 1 + \left( \frac{1 \text{ km}}{p} \right) \left( \frac{M}{M_\odot} \right) \right). \quad (3.33)$$

For an EMRI orbit over a 1-year evolution, the change in the orbital size is approximately  $p \sim (p_0 - 10^{-30})$  km for a realistic  $\Lambda$  value. The expected change in periapsis phase shift due to the SdS gravitational flux is of the order  $\Delta\delta = \delta_{Sch} - \delta_{SdS} \sim 10^{-30}$ . Averaged over an orbital period (single radial cycle)  $P = 2\pi/n(p)$ , the rate of periapsis precession becomes the following expression:

$$\frac{d\delta}{dt} = \frac{\Delta\delta_{1pN}}{P} = \frac{3n(p)}{p} \quad (3.34)$$

which becomes implicitly an osculating orbital element through  $p$  and  $e$ .

Along with the radiation reaction equations, (3.10) and (3.11), which could be interpreted as the (secularly averaged)  $p$  and  $e$  change after a single radial cycle, the complete

adiabatic system are the system of equations:

$$\frac{d\psi}{dt} = n(p)(1 + e \cos \psi)^2 \quad (3.35)$$

$$\frac{d\delta}{dt} = \frac{3n(p)}{p} \quad (3.36)$$

$$\begin{aligned} \frac{dp}{dt} = & -\frac{64}{5}p^{-3}(1 - e^2)^{3/2} \left( 1 + \frac{7}{8}e^2 \right) \\ & - \lambda \left[ 16(1 - e^2) - \frac{4(26e^4 - 283e^2 - 168)}{15(1 - e^2)^{3/2}} + \mathcal{O}(\lambda p) \right] \end{aligned} \quad (3.37)$$

$$\begin{aligned} \frac{de}{dt} = & -\frac{304}{15}p^{-4}e(1 - e^2)^{3/2} \left( 1 + \frac{121}{304}e^2 \right) \\ & - \lambda \left[ \frac{32}{3}p^{-1}e^{-1}(1 - e^2)^{3/2} \left( 1 - (1 - e^2)^{1/2} \right) \right. \\ & \left. - p^{-1}e^{-1} \frac{2(73e^6 - 784e^4 - 965e^2 - 24)}{15(1 - e^2)^{3/2}} + \mathcal{O}(\lambda p^{-2}) \right]. \end{aligned} \quad (3.38)$$

Upon solving for the evolution of the osculating elements, we can reconstruct a sample orbit, with the fast evolution of  $\psi$ , as well as the secular drift of  $\{p, e, \delta\}$ . We note here that the equations for  $\psi$  and  $\delta$  brings about conservative changes to the orbit while the equations for  $p$  and  $e$  comes from the dissipation of energy and angular momentum of the orbit. We present orbital solutions for a selected set of initial conditions,  $(p_0 = 70, \lambda = 10^{-8})$  and  $(p_0 = 50, \lambda = 10^{-7})$  with eccentricities  $e_0 = 0.7$ , and  $e_0 = 0.4$  in Figure 10. Additionally, Figure 11 illustrates the evolution of circular orbits for  $p_0 = 50$  and  $\lambda = 10^{-7}$ . These initial conditions and timestamps were chosen to highlight noticeable orbital deviations induced by the cosmological constant. Beyond accelerating the decrease in binary separation  $r(\psi)$ , the cosmological constant also introduces a phase shift, contributing to enhanced precession of the periapsis.

Lastly, we also estimate the conservative corrections to the orbital period  $P$  due to the cosmological constant.

$$P = \frac{2\pi}{n} = 2\pi \sqrt{\frac{p^3}{GM}} \left( 1 + \frac{\Lambda}{6}p^3 \frac{c^2}{GM} \right) \quad (3.39)$$

where we have brought back the physical constants for increased readability. Considering an EMRI of mass  $\mu = 10M_\odot$  orbiting a black hole of mass  $M = 10^6M_\odot$  in a de Sitter universe with a cosmological constant  $\Lambda \sim 10^{-50}$ , we obtain the following estimate for the orbital period:

$$P \sim 2\pi \times 10^4 \text{ yrs} \left( \frac{p}{1 \text{ pc}} \right)^{3/2} \left( \frac{10^6 M_\odot}{M} \right)^{1/2} \left( 1 + 10^{-18} \left( \frac{p}{1 \text{ pc}} \right)^3 \left( \frac{10^6 M_\odot}{M} \right) \left( \frac{\Lambda}{10^{-50} \text{ km}^{-2}} \right) \right). \quad (3.40)$$

At an orbital separation of 1 pc, the correction from the cosmological constant is negligible. However at much larger separations ( $\mathcal{O}(10^6)$  pc), its effect on the orbital period may become noticeable. Nonetheless, when accounting for gravitational radiation reaction, this correction is further reduced, since the orbital period depends on the evolving orbital size.

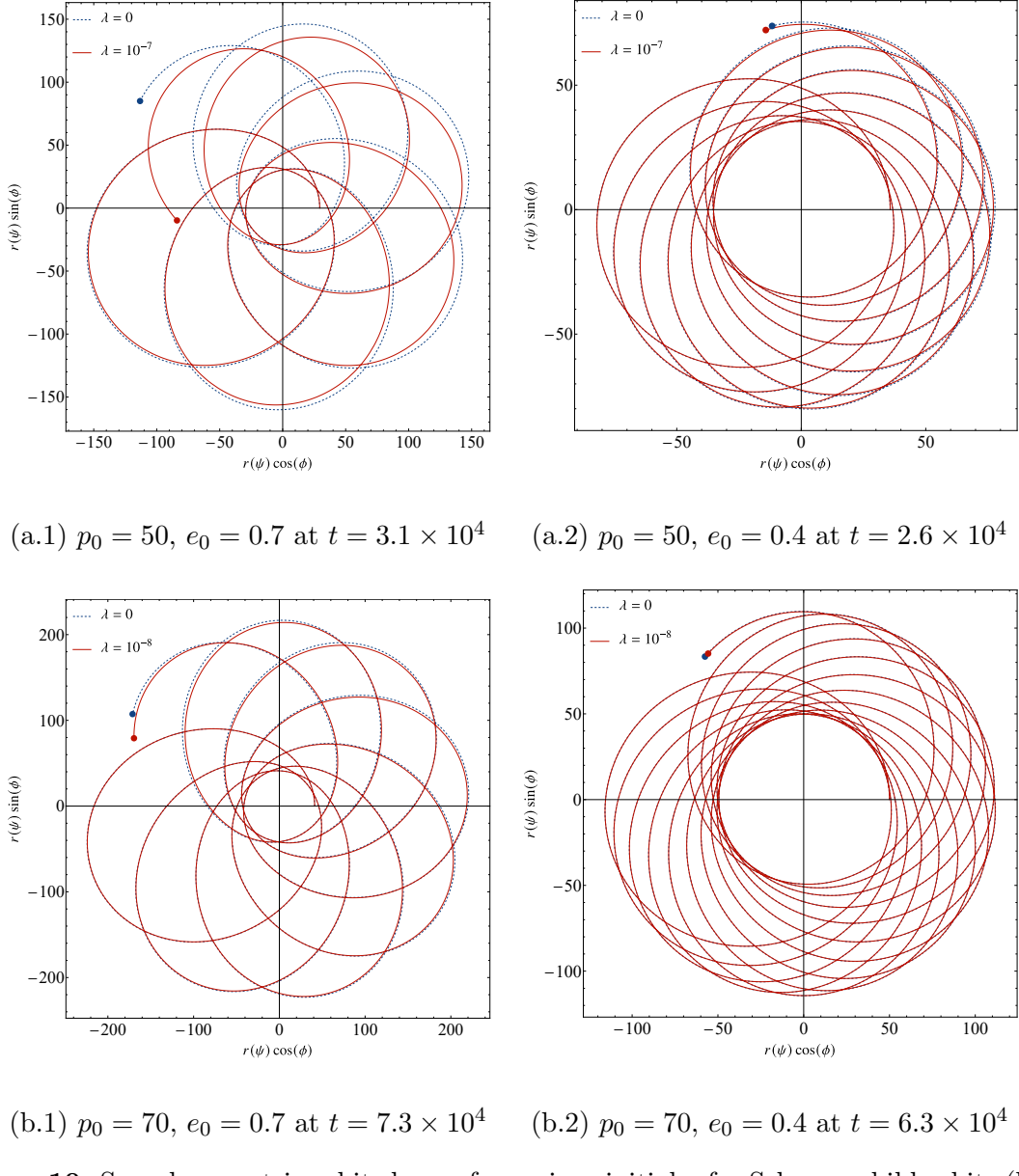


**Figure 10:** Sample eccentric orbit shapes for various initial  $p$  for Schwarzschild orbits (blue, dashed) and for SdS orbits (red, solid) with (a)  $\lambda = 10^{-7}$  and (b)  $\lambda = 10^{-8}$ . The corresponding colored dots are the position at the given time. We show here sample orbital trajectories achievable by initial  $(p_0, e_0)$  indicated below each figure. We also show the time stamps below each figure for the initial parameters to achieve the corresponding orbital shape. We see here that the deviation caused by the cosmological constant is more relevant for orbits of higher eccentricity. We also notice a lag in the phase to complete a radial cycle caused by the cosmological constant.

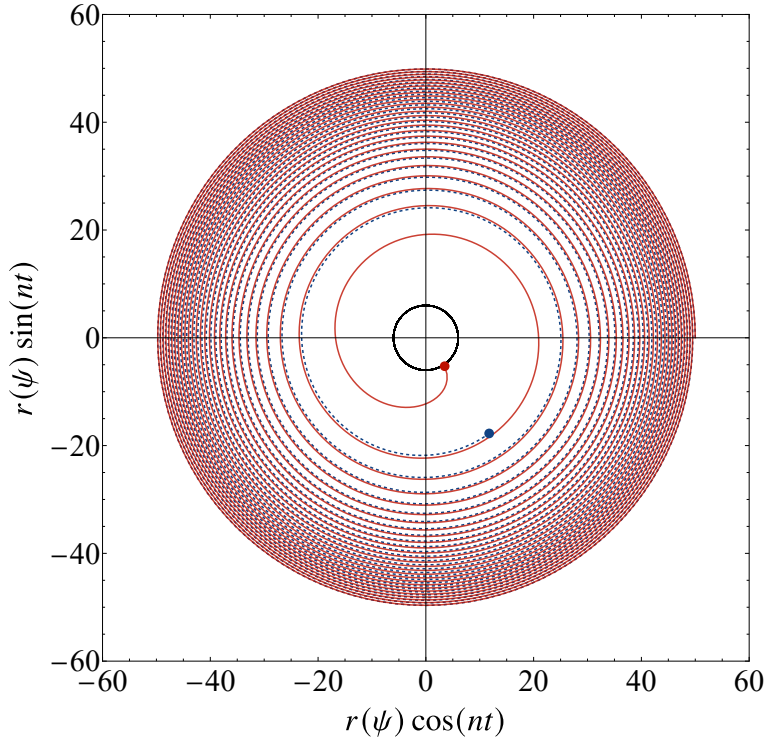


**Figure 11:** Sample circular orbit in Schwarzschild (blue-dashed) and SdS (red-solid) at  $\lambda = 10^{-7}$  spacetime with initial separation  $p_0 = 50$  at times  $t = (0, 1.18 \times 10^5)$ . At short timescales, the orbital deviations are negligible, but at long timescales, SdS orbits deviate noticeably from the Schwarzschild orbit, with the cosmological constant facilitating faster evolution, reaching the separatrix faster (black) or plunging the black hole earlier.

## 4 Gravitational waveforms

In this section, we examine the gravitational waveforms generated by an orbit under adiabatic evolution, where the dominant governing equation is the balance of energy and angular momentum flux. Adiabatic evolution happens when changes in the background metric due to variations in the geodesics are negligible, allowing us to ignore perturbations to the spacetime. The energy and angular momentum flux influences only the orbital parameters, while the trajectory remains constrained to the background geodesics.

### Adiabatic approximation

Adiabatic evolution is defined by the requirement that any relevant orbital parameter  $q = (p, e)$  evolves much more slowly than the radial orbital period  $P = 2\pi/\Omega_r$ , such that  $\Delta q = |\dot{q}|P \ll q$  [56] and  $\Omega_r$  as the radial angular frequency. By analyzing the adiabatic evolution condition, we can effectively divide the full orbital parameter space into two distinct regions:

- *Regions of slow evolution*, where the weak-field gravitational fluxes will be sufficient to describe the evolution of the orbit.
- *Regions of fast evolution*, where a strong-field formalism for energy fluxes (such as black hole perturbation theory) is required, along with corrections to the full metric

to account for changes in the background geodesics (self-consistent evolution with self-force effects).

Adiabatic evolution may still hold in both regions, but as we will see later, additional conditions must be met, imposing further constraints on the orbital parameters.

#### 4.1 Orbits near the separatrix

Near the separatrix, orbits are already expected to be affected by the black hole so strongly that the orbital evolution is described fully by the nonlinearities in the Einstein field equation. This happens when the CO further closes its distance with the black hole continuously, increasing the rate of gravitational energy release. A full computation of the gravitational fluxes in the strong-field regime is beyond the scope of this paper and will be presented in a companion work, where black hole perturbation theory is applied to Schwarzschild - de Sitter spacetime. However, the adiabatic approximation can still be examined in this region to determine the additional conditions necessary for its validity.

We derive the radial period  $P$  near the separatrix,  $p \sim p_{\text{sep}}$  (equation (2.27)) to examine the time scale at which adiabatic evolution holds. Assuming that changes in angular frequency and orbital period remain within the adiabatic limit, we approximate the orbital period at the separatrix up to linear in  $\lambda$  and  $\Delta p \sim p - p_{\text{sep}}$ :

$$P|_{\Delta p \sim p - p_{\text{sep}} \ll 1} \sim 12\sqrt{6}\pi + 3\sqrt{6}\pi \Delta p + \lambda \left( 1296\sqrt{6}\pi + 972\sqrt{6}\pi \Delta p \right). \quad (4.1)$$

We assume here that orbits near the separatrix have already circularized, and we introduce  $\Delta p$  to describe deviations from the separatrix. The validity of the adiabatic approximation is then tested by examining the evolution of  $p$  under the prescribed weak-field fluxes:

$$\frac{|\dot{p}|P}{p} \sim \frac{16}{45}\sqrt{\frac{2}{3}}\pi q - \frac{4}{27}\sqrt{\frac{2}{3}}\pi \Delta p q + \lambda q \left( \frac{56\sqrt{6}\pi}{5} \Delta p + \frac{672\sqrt{6}\pi}{5} \right) \quad (4.2)$$

where we brought back the mass ratio scaling  $q := \mu/M$  from equations (3.10) and (3.11). This leads to a constraint on the mass ratio:

$$\frac{\mu}{M} \sim \frac{45\sqrt{\frac{3}{2}}}{16\pi} + \frac{75\sqrt{\frac{3}{2}}}{64\pi} \Delta p - \lambda \left( \frac{25515\sqrt{\frac{3}{2}}}{8\pi} + \frac{93555\sqrt{\frac{3}{2}}}{32\pi} \Delta p \right). \quad (4.3)$$

We now assess whether the mass ratio constraint can remain within the physical range  $q \in (0, 1)$ . In the absence of a cosmological constant ( $\lambda = 0$ ), the constraint leads to unphysical scenarios, producing values outside the range of  $q$  for  $\Delta p$ , i.e., for  $p > p_{\text{sep}}$ . This invalidates the use of weak-field fluxes for adiabatic evolution in the strong-field region. Furthermore, inclusion of a cosmological constant does not help loosen the validity of this approximation; for the constraint to yield physically meaningful mass ratios, an unrealistically large cosmological constant ( $\lambda \sim 10^{-3}$ ) well beyond the bound for stable orbits ( $\lambda \sim 10^{-4}$ ). Although the breakdown of our initial assumptions (such as the applicability of pN fluxes near the separatrix) suggests that this analysis is not strictly valid in the strong-field regime, this calculation serves as a preliminary attempt to explore the influence of the cosmological constant on the limits of adiabatic evolution.

We now present preliminary results comparing the weak-field energy flux formula with the strong-field energy flux at infinity, obtained from the perturbation of spherically symmetric spacetimes due to an orbiting point mass. This comparison provides insight into the validity range of the weak-field formula. The strong-field energy flux is obtained using methods of Schwarzschild perturbation theory [75–77], generalized to spherically symmetric spacetimes to accommodate the Schwarzschild-de Sitter spacetime. We briefly outline the method, with the complete procedure detailed in a companion paper. The goal is to numerically calculate the energy flux valid near the separatrix of the Schwarzschild-de Sitter spacetime:

$$\langle \dot{E}_{\ell m}^{\infty} \rangle = \frac{1}{64} \frac{(l+2)!}{(l-2)!} \sum_n \omega_{mn}^2 |C_{\ell mn}^+|^2. \quad (4.4)$$

Here  $\omega_{mn}$  is the angular frequency of the orbiting particle in terms of the  $(m, n)$  modes of its radial and azimuthal oscillations. The normalization coefficient  $C_{\ell mn}^+$  is obtained by numerically integrating the inhomogeneous Regge-Wheeler-Zerilli equation in the frequency domain with the tortoise coordinate defined by  $\frac{dr}{dr_*} = f^{-1}$ ,

$$\left( \frac{d^2}{dr_*^2} - V_{\ell} + \omega_{mn}^2 \right) R_{\ell mn}(r) = Z_{\ell mn}(r) \quad (4.5)$$

where  $R_{\ell mn}$  satisfies the general solution of the form:

$$R_{\ell mn}(r) = c_{\ell mn}^+(r) \hat{R}_{\ell mn}^+(r) + c_{\ell mn}^-(r) \hat{R}_{\ell mn}^-(r) \quad (4.6)$$

with the coefficients defined as:

$$\begin{aligned} c_{\ell mn}^+(r) &\equiv \frac{1}{W_{\ell mn}} \int_{r_{\min}}^r dr' \frac{\hat{R}_{\ell mn}^-(r') Z_{\ell mn}(r')}{f(r')}, & C_{\ell mn}^+ &\equiv c_{\ell mn}^+(r_{\max}) \\ c_{\ell mn}^-(r) &\equiv \frac{1}{W_{\ell mn}} \int_r^{r_{\max}} dr' \frac{\hat{R}_{\ell mn}^+(r') Z_{\ell mn}(r')}{f(r')}, & C_{\ell mn}^- &\equiv c_{\ell mn}^-(r_{\min}). \end{aligned} \quad (4.7)$$

The source term  $Z_{\ell mn}(r)$  is derived from the stress-energy tensor of a point particle, of mass  $\mu$ , in a generic orbital trajectory,  $x_p(\tau)$ :

$$T^{\mu\nu}(x^\alpha) = \mu \int \frac{d\tau}{\sqrt{-g}} u^\mu(\tau) u^\nu(\tau) \delta^4[x - x_p(\tau)]. \quad (4.8)$$

The homogeneous solutions  $\hat{R}_{\ell mn}^{\pm}(r)$  are obtained by solving the homogeneous Regge-Wheeler-Zerilli equation with the following asymptotic ingoing and outgoing wave boundary conditions:

$$\hat{R}_{\ell mn}^{\pm}(r_* \rightarrow \pm\infty) = \exp(\pm i\omega_{mn} r_*). \quad (4.9)$$

Although this method allows for a generic orbital configuration, we restrict the preliminary analysis to the circular limit and consider only the dominant  $(l, m)$  energy flux mode. This simplification is sufficient to provide a rough verification of the weak-field formula. Specifically, we solve for  $E_{22}^{\infty}$  using the Zerilli potential, modified to incorporate the cosmological constant (with the full derivation included in the companion paper):

$$V_{\text{even}} = \frac{f}{r^2 \tilde{\Lambda}^2} \left[ 2\tilde{\lambda}^2 \left( \tilde{\lambda} + 1 + \frac{3M}{r} \right) + \frac{18M^2}{r^2} \left( \tilde{\lambda} + \frac{M}{r} \right) \right] - \frac{f}{r^2 \tilde{\Lambda}^2} (6M^2 \Lambda) \quad (4.10)$$

with constants (not related to  $\lambda$  or  $\Lambda$ )  $\tilde{\Lambda} = \tilde{\lambda} + 3M/r$  and  $\tilde{\lambda} = (l+2)(l-1)/2$ .

We note here however, that (4.4) is the expected radiation rate if the spacetime is asymptotically flat. This is a problem since we know that SdS is asymptotically de - Sitter, and the energy flux in terms of the fields should be modified by the cosmological constant. Luckily, many prescriptions on computing the energy flux have been put forward by analyzing de Sitter in Bondi frame, and computing the mass loss in terms of the news tensor, notably by [41, 45, 78] and more recently, de Sitter quadrupolar linearized waves by [46, 79, 80]. It was shown that the even parity,  $\ell = 2$  fields (at the Bondi frame of the asymptotically de Sitter null infinity) carry energy far from the source,  $r \rightarrow \infty$ , (a la' Teukolsky waves [81]) as

$$\dot{E}^{\ell=2,m=\pm 2} = -\frac{3}{8\pi G} \left| \partial_u^3 A_m - \frac{4}{3} \Lambda \partial_u A_m \right|^2 - \Lambda |\partial_u^2 A_m|^2 + \mathcal{O}(\Lambda^2) \quad (4.11)$$

where  $A_m(u)$ 's are even-parity solutions to the linearized Einstein field equations that reduces to the asymptotically flat limit at  $\Lambda \rightarrow 0$ . Throughout our energy flux comparisons, we only use the asymptotically flat limit of the energy flux formula, since all succeeding terms from the  $\Lambda$  correction have subdominant contributions compared to the leading term.

The energy flux computed from the solutions of the Regge-Wheeler-Zerilli equations is expected to be independent to a far-field (large- $p$ ) approximation, as these equations are derived from perturbations of the SdS spacetime due to an orbiting test mass. Hence, the strong-field energy flux formula should remain valid even at large orbital separations. This allows us to assess the accuracy of the weak-field energy flux formula (equation (3.3)) by evaluating its deviation from the strong-field energy flux (equation (4.4)).

In Figure 12, we illustrate the deviation of the energy flux obtained from perturbation theory (equation (4.4)) and that from a weak-field expansion (equation (3.3)),  $1 - |\dot{E}_{22}^\infty / \dot{E}_{pN}|$ , for increasing binary separation,  $r_p$ , and cosmological constant,  $\lambda$ . We also compare the energy flux of circular orbits to eccentric orbits, showing the deviations in Figure 13. Our results indicate that for higher values of  $\lambda$ , significant deviations emerge at sufficiently large  $r_p$ , confirming that the weak-field quadrupolar energy flux (equation (3.3)) remains valid only within the particle position satisfying the hierarchy (equation (2.33)). Additionally, for smaller  $\lambda$ , the OSCO shifts farther from the black hole, leading to an increasingly larger region of validity for the weak-field fluxes. Overall, we find that higher  $\lambda$  values lead to a scaling error in eccentric orbits relative to their circular counterparts. However, as expected, for smaller  $\lambda$ , both circular and eccentric orbits exhibit similar deviations in the fluxes.

## 4.2 Orbits far away from the separatrix

It has been shown that in regions far from the separatrix, and thus the black hole, applying adiabatic approximation on orbital evolution results to no strict conditions for the mass ratio of the binary [56]. We repeat the analysis here to determine whether the presence of a cosmological constant introduces new constraints. Similar to the derivation from previous subsection, the change in the semi-latus rectum in the large- $p$  limit yields the following constraint on the mass ratio:

$$\frac{\mu}{M} \ll \alpha(e)p^{5/2} - \lambda(\beta(e)p^{11/2} + \mathcal{O}(\lambda p^{7/2})) \quad (4.12)$$

where  $\alpha(e)$  and  $\beta(e)$  are positive functions of eccentricity for all values of  $e$ . This result confirms that the constraint is automatically satisfied for large  $p$ , implying that the validity of the weak-field fluxes for adiabatic evolution remains independent of the mass ratio. Hence,

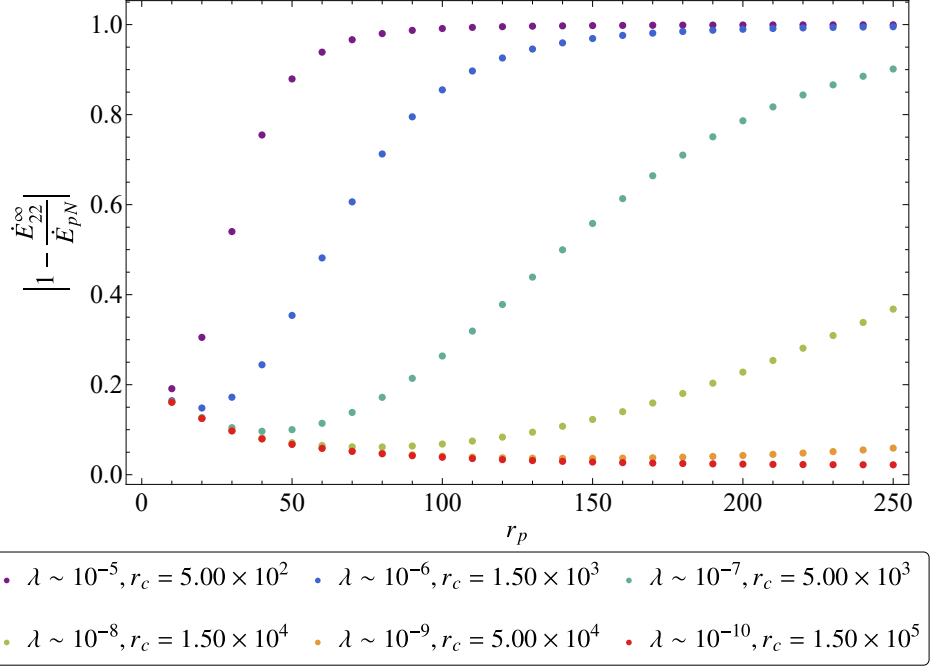


**Figure 12:** Deviation of the weak-field energy flux formula (equation (3.3)) and the strong field energy flux ( $l = 2, m = 2$  mode) from SdS perturbation theory (equation (4.4)) for a circular orbit of radius  $r_p$ . The validity of the weak-field energy flux formula is stronger for larger  $r_p$  and lower  $\lambda$ . For smaller  $r_p$ , the weak-field formula may still be valid if  $\lambda$  is allowed to be of lower value.

at large distances, the evolution of the orbital parameters is necessarily adiabatic. We note however that the presence of a cosmological constant  $\lambda$  strengthens the bound at which adiabaticity may be applied to eccentric orbits. This suggests that in the case of eccentric orbits, the strong-field region is effectively shifted towards much lower  $p$ . Thus, the weak-field fluxes will be sufficient for the balance formula governing the orbital trajectory and gravitational waveforms.

We present below the gravitational waveforms, deriving the phase from the orbital mean motion and the strain magnitude from the binary mass quadrupole moment. The leading order relationship of the time derivatives of the mass quadrupole moment to the waveform strain will be sufficient to show the effect of the cosmological constant up to order  $\Lambda^{1/2}$  since the linearized radiation in asymptotically-de Sitter spacetime was shown to be [43, 82]:

$$\chi_{ij} \sim \partial_t^2 Q_{ij} + \mathcal{O}\left(\frac{\sqrt{\Lambda}}{D}\right) \quad (4.13)$$

with  $D$  as the wave zone distance. The wave zone radiation was derived from the perturbation of de Sitter spacetime (with the cosmological constant related to  $H$  by  $H^2 = \Lambda/3$ ),

$$g_{\mu\nu} = \gamma_{\mu\nu} + \epsilon h_{\mu\nu} \quad (4.14)$$

with the background line element,

$$\gamma_{\mu\nu} dx^\mu dx^\nu = -dt^2 + e^{2Ht} \delta_{ij} dx^i dx^j \quad (4.15)$$

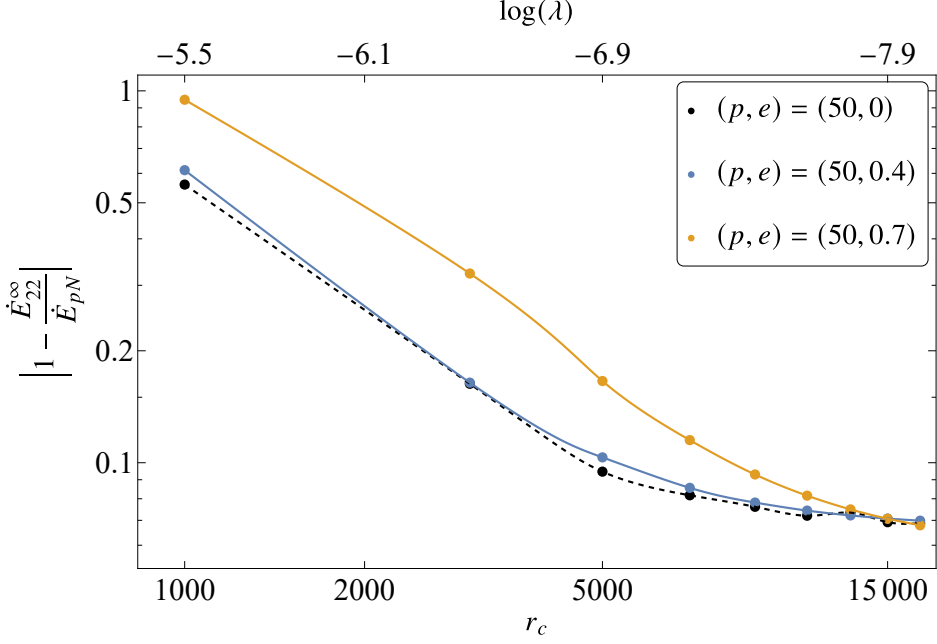


**Figure 13:** Deviation of the weak-field energy flux formula (equation (3.3)) and the strong field energy flux ( $l = 2, m = 2$  mode,  $n_{max} = 30$ ) from SdS perturbation theory (equation (4.4)) for generic eccentric orbits in terms of the cosmological constant,  $\lambda$ , and cosmological horizon,  $r_c$ .

which should be valid far from the source. The resulting linearization of the field equations has the following form,

$$\eta^{\alpha\beta}\partial_\alpha\partial_\beta\chi_{\mu\nu} + \frac{2}{\eta^2}\partial_0\chi_{\mu\nu} - \frac{2}{\eta^2}\left(\delta_\mu^0\delta_\nu^0\eta^{\alpha\beta}\chi_{\alpha\beta} + \delta_\mu^0\chi_{0\nu} + \delta_\nu^0\chi_{0\mu}\right) = -16\pi T_{\mu\nu} \quad (4.16)$$

with  $\eta_{\mu\nu}$  as the components of the Minkowski metric, and with the radiation field

$$\chi_{\mu\nu} = \exp(-2Ht)\bar{h}_{\mu\nu} \quad (4.17)$$

with  $\bar{h}_{\mu\nu}$  as the usual trace-reversed perturbation metric. The radiation field can then be expressed in terms of the source multipole moments,

$$\begin{aligned} \chi_{ij} = & \frac{2}{R}\left(e^{-Ht} + HR\right)\left[\dot{Q}_{ij}^{(\rho)} - 2H\dot{Q}_{ij}^{(\rho)} + H\dot{Q}_{ij}^{(p)}\right] \\ & - 2H\left[\ddot{Q}_{ij}^{(\rho)} - 3H\dot{Q}_{ij}^{(\rho)} + H\dot{Q}_{ij}^{(p)} + 2H^2Q_{ij}^{(\rho)} - H^2Q_{ij}^{(p)}\right]. \end{aligned} \quad (4.18)$$

with  $R$  as the radial distance of the source,  $R^2 = x^2 + y^2 + z^2$ . Higher order terms in  $\Lambda$  would represent tail terms in the waveform due to backscattering [42], which we will ignore here since their contribution to the amplitude and phase is small enough with respect to the leading order. At spatial infinity, the polarization modes of the gravitational wave signal  $h$  (in the transverse-traceless gauge), at a distance  $D$  from the source, will then be related to the mass quadrupole moment (we suppress the label  $\rho$ ,  $Q_{ij}^{(\rho)} = Q_{ij}$ ), as it is in an asymptotically

flat spacetime (up to leading order in  $\Lambda$ ) [71, 82] by the following expression:

$$h_+ = \frac{1}{D} \left( \ddot{Q}_{11} - \ddot{Q}_{22} + 2\sqrt{\frac{\Lambda}{3}} (\dot{Q}_{11} - \dot{Q}_{22}) \right) + \frac{\Lambda}{3} \left( \dot{Q}_{11} - \dot{Q}_{22} + \frac{2\sqrt{\Lambda}}{3} (Q_{11} - Q_{22}) \right) \quad (4.19)$$

$$h_\times = \frac{2}{D} \left( \ddot{Q}_{12} - 2\sqrt{\frac{\Lambda}{3}} \dot{Q}_{12} \right) + \frac{\Lambda}{3} \left( \dot{Q}_{12} - 2\sqrt{\frac{\Lambda}{3}} Q_{12} \right). \quad (4.20)$$

We assume that the binary components lie in a single plane, say the  $x - y$  plane, and the observer is aligned along the  $z$ -axis. This orientation corresponds to a face-on view of the binary. We further set the orbital plane such that its origin coincides with one of the foci of the elliptic orbit, which would be the position of the central black hole. The mass quadrupole moment of the binary, with reduced mass  $\mu$ , is then expressed into:

$$Q_{ij} = \mu r^2(\psi) \begin{pmatrix} \cos^2(\phi) & \sin(\phi) \cos(\phi) & 0 \\ \sin(\phi) \cos(\phi) & \sin^2(\phi) & 0 \\ 0 & 0 & 0 \end{pmatrix}. \quad (4.21)$$

Substituting in the solutions of the adiabatic osculating trajectory equations into the strain formulas (4.20), allows us to generate adiabatic waveforms plots valid in the weak-field region of the parameter space. It would also be sufficient to plot the polarization strains (4.20) up to the leading order in  $\Lambda$  (ignoring the second term) since we are already using the leading  $\Lambda$ -corrected solutions in the orbital parameters. We note here that under secular evolution [83], the waveform phase would gain additional contribution from the conservative gravitational self-force, which we do not include in this paper.

In Fig. 14, we present a circular waveform under the assumption that the orbit begins with a small initial eccentricity and circularizes almost instantly, making  $\dot{e}$  negligible. We observe an phase advance, which can be attributed to the cosmological constant term in the mean motion.

This early departure arises from modified angular frequency, with the energy and angular momentum being affected by the cosmological constant the most for nontrivial eccentricities.

Lastly, we estimate the change both in the amplitude and the phase of the waveform due to the SdS gravitational flux in an EMRI orbit. We begin by considering the analytical expression for complex time-domain waveform [71]:

$$h(t) = \mathcal{A}(t) \exp(i\Psi(t)) = h_+ - i h_\times \quad (4.22)$$

where the SdS change in amplitude arises from an  $\mathcal{O}(\lambda)$  deviation,  $\delta\mathcal{A}_{SdS}$ , in the amplitude

$$\mathcal{A} = \mathcal{A}_{pN}(1 + \delta\mathcal{A}_{SdS}). \quad (4.23)$$

Similarly, the phase correction,  $\delta\Psi_{SdS}$ , appears in

$$\Psi = \Psi_{pN}(1 + \delta\Psi_{SdS}). \quad (4.24)$$

The post-Newtonian amplitude and phase are related to the Keplerian frequency  $\omega_N$  as  $\mathcal{A}_{pN} = 4\omega_N^{2/3}/D$  and  $\Psi_{pN} = 2\omega_N t$ . Expressing the semi-latus rectum  $p$  in terms of  $\omega_N$

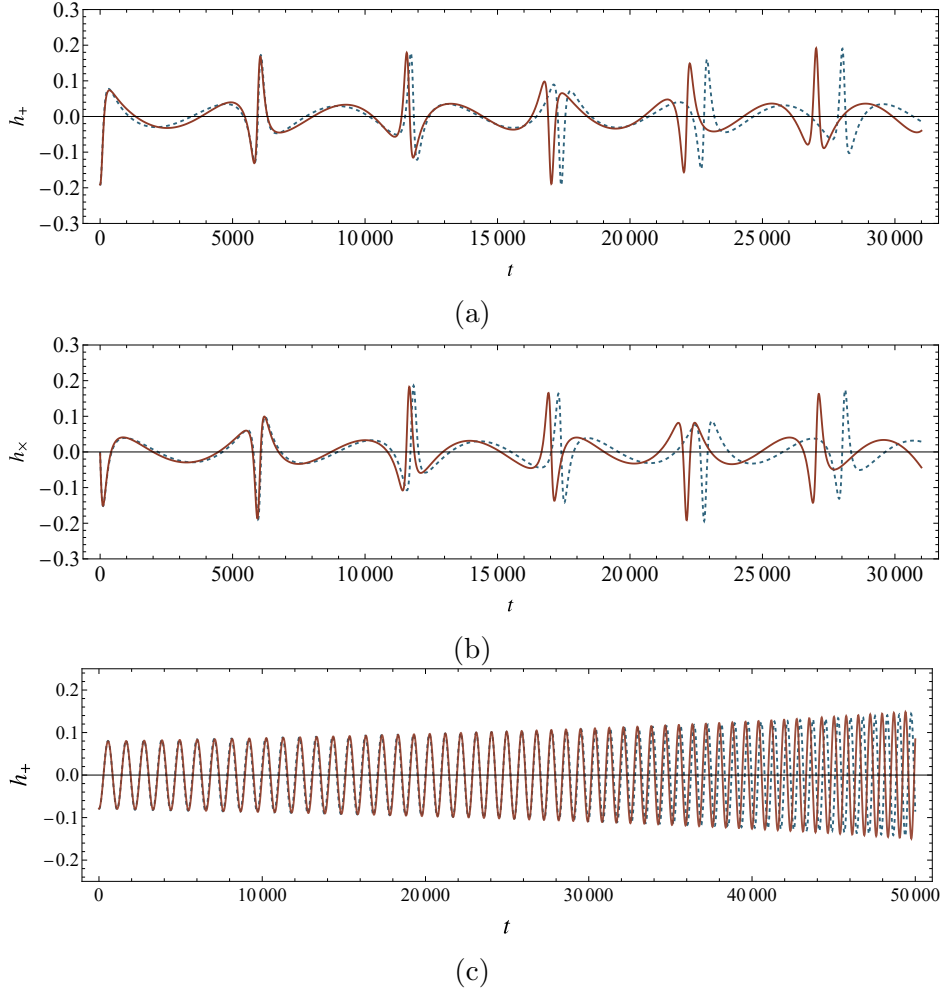


**Figure 14:** Adiabatic waveforms of ( $p_0 = 50$ ) for Schwarzschild with  $\lambda = 0$  (dashed, blue) and with SdS with  $\lambda = 10^{-7}$  (red). We show here the (a) plus polarization as well as the (b) cross polarization of the waveform in the adiabatic limit of an initially eccentric orbit with eccentricity  $e_0 = 0.7$ . We show here the plus polarization (c) of the waveform in the adiabatic limit of an initially circular orbit. The main effect of the cosmological constant is the increase in amplitude and an initial delay in the wave phase.

via  $\omega_N = p^{-3/2}$  and using the evolution equations (equations (3.10) and (3.11)) we obtain first-order SdS corrections:

$$\delta \mathcal{A}_{SdS} = -\lambda \omega_N^{-2} + \mathcal{O}(\lambda^2) \quad (4.25)$$

$$\delta \Psi_{SdS} = -\lambda \frac{\omega_N^{-2}}{2} + \mathcal{O}(\lambda^2). \quad (4.26)$$

These expressions indicate that the amplitude and phase shift are initially small but grow as the frequency increases. This suggests that both the amplitude and phase of the SdS waveform will eventually deviate significantly from their pN counterparts at an earlier stage

in the inspiral. The Keplerian mean motion,  $\omega_N$  may be estimated as:

$$\omega_N \sim 1.22 \times 10^{-4} \text{yr}^{-1} \left( \frac{1 \text{ pc}}{p} \right)^{3/2} \left( \frac{M}{10^6 M_\odot} \right)^{1/2}. \quad (4.27)$$

Since both amplitude and phase shifts scale similarly with  $\omega_N$ , we then obtain an estimate for  $\delta\mathcal{A}_{SdS}$  and  $\delta\Psi_{SdS}$  in a circular EMRI:

$$\delta\mathcal{A}_{SdS} \sim \delta\Psi_{SdS} \approx 10^{-18} \left( \frac{p}{1 \text{ pc}} \right)^3 \left( \frac{M}{10^6 M_\odot} \right) \left( \frac{\Lambda}{10^{-50} \text{km}^{-2}} \right). \quad (4.28)$$

Using the previous inspiral rate estimate (equation (3.22)), a circular inspiral over one year causes a decrease of  $p \approx 10^{-25}$  km, leading to an extremely small reduction in the amplitude of order  $\mathcal{O}(10^{-93})$ . However, as the frequency increases, the amplitude and phase shift eventually surpass their pN counterparts at critical frequency,  $\omega_{crit} \sim \lambda^{-1/2}$ . Before reaching  $\omega_{crit}$ , the cosmological constant primarily reduces the amplitude of the waveform and delays the phase evolution. For initially eccentric orbits, the phase shift remains similar to the circular case, since we consider the waveform frequency to be related to the mean motion averaged over a full orbit. However, the amplitude shift is modified by the eccentricity:

$$\mathcal{A}(e)D = \frac{2(e+2)\omega^{2/3}}{(e+1)^3} - \lambda \frac{4}{\omega^{4/3}(e+1)^2} + \mathcal{O}(\lambda^2) + \mathcal{O}(\omega^{4/3}). \quad (4.29)$$

We see in this expression that more eccentric orbits produce a lower overall amplitude shift due to the cosmological constant compared to circular orbits. The eccentricity affects  $\omega_{crit}$  at most by a factor of order  $e$ , which increases for higher eccentricities. As a consequence, waveforms from highly eccentric SdS orbits take longer to surpass the amplitude and phase of their circular waveform counterparts.

## 5 Timescales for gravitational wave detection

In this section, we apply the radiation reaction equations (equations (3.10) and (3.11)) to estimate the inspiral timescales for gravitational wave detection. Detectors will be operating for only a limited amount of time and therefore can only detect transient gravitational wave signals from sources for a given range of lengthscale or timescale. For the space-based detector LISA, the operation time is only up to 4.5 years before closing down for improvements [17, 84]. Signals can only enter the detector frequency range and can be detected at the “lifetime” of the detector, which can translate to sources up to a range of length or timescale. Sources that plunge less than the detector lifetime as well as those that cannot reach the frequency of the detector bandwidth will be irrelevant sources for detection. It will then be important to predict sources in a specific range of orbital parameters that can decay in a specific time. In this section, we obtain an analytical inspiral timescale formula in terms of orbital parameters that can describe the decay of a binary, similar to what was derived by [72] and extract what effect the cosmological constant may bring.

For circular orbits, an exact analytic decay timescale with the effect of the cosmological constant can be derived similarly in [72]. Peters’ argument of minimal dependence of  $e(p)$  can also be used to extend the suitability of the timescale to eccentric orbits. We start by deriving the inspiral timescale as the integral of the inverse of the  $\dot{p}$  equation. Integrating up to near-coalescence, the timescale,  $\tau$ , becomes a function of the initial orbital parameters.

Up to  $\mathcal{O}(\lambda)$ , the timescale with a cosmological constant is derived as a factor multiplied to Peters' timescale  $\tau_P$ ,

$$\tau \sim \tau_P (1 + \lambda \tau_\lambda) \quad (5.1)$$

with Peters timescale in  $(p, e)$  space is equal to

$$\begin{aligned} \tau_P &= \frac{5c^5 p_0^4}{256G^3 M^3 q f(e_0)} \\ &= 1.84 \times 10^{24} \text{yr} \left( \frac{p_0}{1 \text{pc}} \right)^4 \left( \frac{10^6 M_\odot}{M} \right)^3 \left( \frac{10^{-5}}{q} \right) \frac{1}{f(e_0)} \end{aligned} \quad (5.2)$$

wherein we brought back the physical units and scalings for increased readability. The semi-latus rectum  $p$  here has units of length unlike the previous usage of the nondimensional  $p$ . The function  $f(e_0)$  is the enhancement function for including initially eccentric orbits, and is equal to:

$$f(e) = (1 - e^2)^{3/2} (1 + 7e^2/8). \quad (5.3)$$

The timescale function linear to  $\lambda$  is given by:

$$\tau_\lambda = -\frac{19c^2 p_0^3}{4GM} \frac{F(e_0)}{f(e_0)} \quad (5.4)$$

which is related to a new eccentricity enhancement function:

$$F(e) = \frac{1}{228(1 - e^2)^{3/4}} \left( 60(1 - e^2)^{5/4} - 26(1 - e^2) - 231\sqrt{1 - e^2} + 425 \right) \quad (5.5)$$

that evaluates to 1 for  $e \rightarrow 0$ . For circular orbits, we have the timescale ratio  $\sigma(p, e = 0, \lambda) = \tau_P/\tau$  has the form:

$$\begin{aligned} \sigma(p_0, e = 0, \lambda) &= 1 - \lambda \frac{19c^2 p_0^3}{4GM} + \mathcal{O}(\lambda^2) \\ &= 1 - \lambda \frac{19}{4} \left( \frac{p_0}{1.5 \text{ km}} \right)^3 \left( \frac{1M_\odot}{M} \right)^3. \end{aligned} \quad (5.6)$$

The main effect of the factor is to reduce the timescale due to the negative sign. Larger initial orbits will have an increased deviation to the Peters' timescale due to the  $p_0^3$  scaling. As the orbiter starts initially near the BH, it will approximately follow the Peters' timescale but if it starts initially farther, the timescale correction goes larger as shown in Figure 15. For a stellar mass BH, with mass  $M = \mathcal{O}(10)M_\odot$ , circular orbits will decay in a timescale reduced by a factor of  $\sigma \approx 1 - 10^{-3}\lambda p_0^3$ , which will only become considerably large if the starting orbit has a size  $p_0 \approx 10\lambda^{-1/3}$  km. Near the maximum cosmological constant, say  $\lambda = 10^{-6}$ , the starting orbit must be around  $p_0 \sim \mathcal{O}(10^3)$  km to have maximum deviation. Beyond this estimate, the ratio will be negative and is thus unphysical, which means that orbits are unbound at these regime. For a SMBH, the correction is very small with an initial orbit having  $p_0 \sim \mathcal{O}(10^8)$  km before being considerably large. This may be of astrophysical significance for scenarios of large-distance capture of inspiralling objects like EMRIs by SMBH [84, 85] with gravitational wave induced evolution estimated to be the dominant dynamics starting at a relatively large distance. We note here that a  $\lambda = 10^{-6}$  means either a relatively

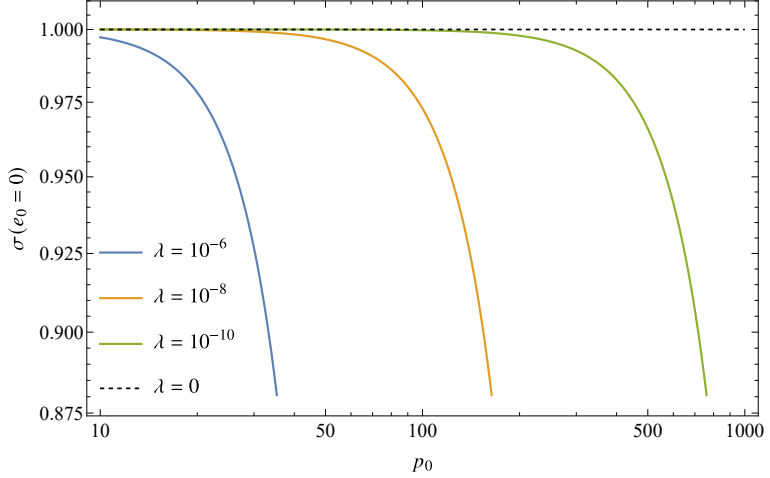


**Figure 15:** Ratio,  $\sigma(p_0, \lambda)$ , of the Peters-Mathews inspiral timescale and the full SdS inspiral timescale for various cosmological constant values with its  $p$  dependence and (b) its  $e$  dependence. We see here that larger orbits gain an increased effect by the cosmological constant as the orbit will decay faster compared to the Peters' decay time ( $\lambda = 0$ ).

small  $\Lambda$  ( $= 10^{-18}$ ) compared to the measured  $\Lambda$  ( $\sim 10^{-50}$ ) [86] or hypothetically large black hole (of order  $M = 10^{22} M_\odot$ ) inside a small universe (of order  $\mathcal{O}(10^9)$  km).

For the effect of the eccentricity, let us include the enhancement functions from equations (5.3) and (5.5). To obtain this, we only need to multiply the earlier factors to the  $\Lambda$  dependent term,

$$\sigma(p_0, e_0, \lambda) \sim 1 - \lambda \frac{19c^2 p_0^3}{4GM} \frac{F(e)}{f(e)}. \quad (5.7)$$

The deviation,  $\tau(e) - \tau(e = 0)$ , brought by the eccentricity can also be visualized by noticing that the correction factor to the timescale is just the eccentricity functions:

$$\frac{\tau_P(e)}{\tau_P(e = 0)} = f(e_0)^{-1}, \quad (5.8)$$

$$\frac{\tau_\lambda(e)}{\tau_\lambda(e = 0)} = F(e_0)/f(e_0). \quad (5.9)$$

We show in Figure 16 the comparison of  $f(e_0)^{-1}$  and  $F(e_0)/f(e_0)$ . The function  $F(e_0)/f(e_0)$  increases faster than  $f(e_0)$  for more eccentric orbits which means that the effect of eccentricity in modifying the timescale is strengthened by the presence of the cosmological constant. We see in Figure 16 that an initially eccentric orbit, with  $e_0 \sim 0.7$ , the deviation to the inspiral timescale is strengthened to a factor of  $\mathcal{O}(100)$ . This can also mean that as the eccentricity continues to decrease, the value of eccentricity affects the SdS inspirals faster as compared to pN inspirals.

We show in Figure 17 the cosmological constant contours and isochrones in the phase space of orbital parameters  $(p, e)$ . If we relate the area in the phase space as the number of potential sources, Figure 17(a) shows that higher values of cosmological constant increases the population of detectable sources at a fixed inspiral time. In Figure 17(b) we see that the SdS inspiral time shows a different curve from the  $\lambda = 0$  inspiral time implying a shift in the orbital parameters of potential sources. This means that for a given time, we can detect

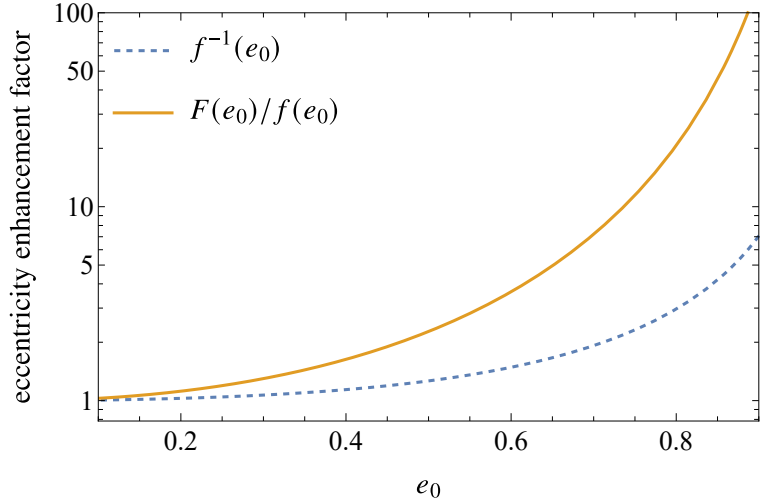


**Figure 16:** Eccentricity factors for the circular inspiral time. We see here that initially eccentric orbits are more affected by the cosmological constant which can result to a larger deviation in the decay time with Peters formula. Up to a factor of  $\sim 100$  is to be included for  $e_0 \sim 0.7$  orbit decay time. However, this will still scale with the value of  $\lambda$  linearly.

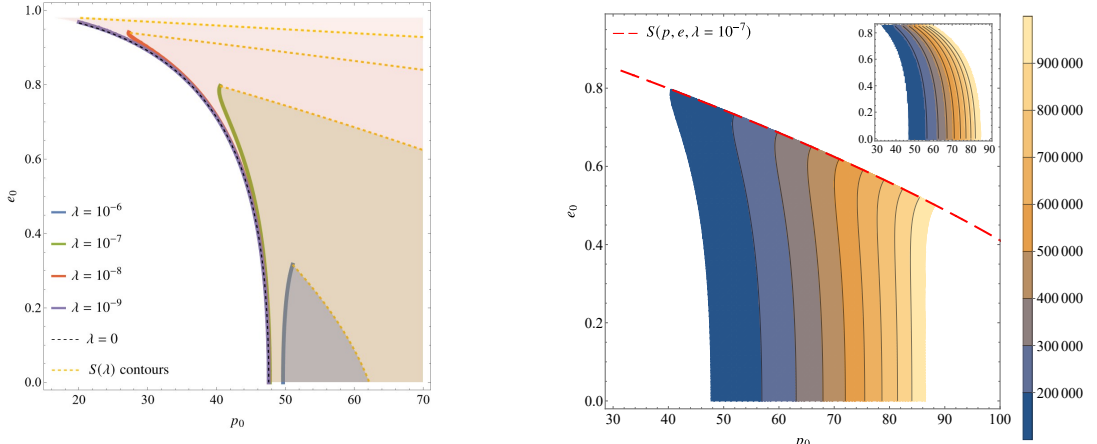
much larger orbits due to the cosmological constant. The general observation here is that the population of sources will be limited to their initial eccentricity and size at capture and will increase due to higher eccentricity with larger orbits decaying faster from the effect of the cosmological constant.

We can now numerically integrate the orbital evolution equations to obtain a more realistic inspiral time measurement across the parameter space. We start by solving the plunge times for a range of initial parameters, then we deduce if those parameters are detectable within a given time. We numerically integrate the radiation reaction equations (equations (3.10) and (3.11)), considering all possible initial parameters at a given range. Then we stop the integration if the parameters near the separatrix and we then collect the time per initial parameter for the integration to end. We consider the range  $p_0 = (10, 50)$ ,  $e_0 = (0, 1)$  with the cosmological constant near maximum,  $\lambda = 10^{-7}$ . The isochrones with the evolving eccentricity is obtained numerically in Figure 18. We show in Figure 18 that for a given range of time, the range of initial parameters is expanded due to the presence of a cosmological constant. Orbits of the same size will indeed decay faster with the help of the cosmological constant, but the higher the eccentricity, the factor of reduction in the timescale is decreased.

## 6 Conclusions

The cosmological constant introduces both conservative and dissipative effects on the dynamics of a binary system. Key findings of this paper include an accelerated rate of orbital decay, with shorter plunge and circularization times due to the cosmological constant. Additionally, we demonstrate that eccentric orbits are more strongly influenced by the cosmological constant, with this effect being independent of the binary's separation.

For the conservative effects, we analyze changes in the effective potential, where the cosmological constant introduces additional turning points for a given orbital parameter. Depending on its value, the cosmological constant alters the nature of bound and unbound



(a) Contours of equal  $\lambda$  for a fixed inspiral time.

(b) Isochrones for a fixed  $\lambda$

**Figure 17:** Analytical contours for a fixed  $\tau$  and fixed  $\lambda$ . In (a), we have an increasing  $\lambda$  for a fixed  $\tau = 10^5$  with the filled region as the source population with higher decay timescale ( $\tau > 10^5$ ). The fixed timescale contours show that by increasing the cosmological constant, the total area covered by a particular timescale contour decreases which could mean that the source population will decrease most notably in  $e$  for a given cosmological constant and time. However in (b), we compare decreasing  $\tau$  for a fixed  $\lambda$ , and by comparing timescale contours for a specific cosmological constant, the source population increases in  $p$  as compared to the  $\lambda = 0$  case.

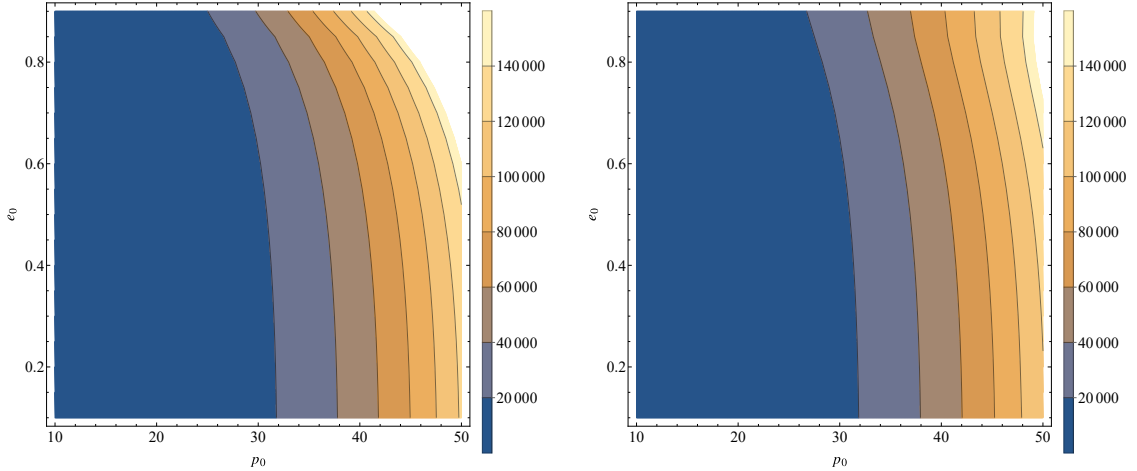


**Figure 18:** Numerical contour plots of the plunge times in a range of initial orbital parameters for Schwarzschild ( $\lambda = 0$ ) (left) and SdS ( $\lambda = 10^{-7}$ ) (right) spacetime. We note here that incorporating a self-consistent evolution in  $(p, e)$  decreases plunge times as the CO starts to inspiral further away from the BH. Given a fixed timescale, say at  $\tau = 10^5$ , a larger region is covered in the initial parameter which can be expected as an increase in the population of potential gravitational waves sources. There is also notable decrease in population for highly eccentric orbits as also seen from the analytical contours previously, which means that highly eccentric orbits will be expected to decay slower as compared to higher values of cosmological constant.

orbits, with a critical threshold causing the complete absence of bound orbits. This leads to an analysis of the cosmological constant’s influence on the orbital parameters governing the existence of bound orbits. We derive the separatrix, represented as a 2D surface, a polynomial function of  $(p, e, \lambda)$ , and identify the critical value of the cosmological constant that allows for a single stable bound orbit. Although small in magnitude, the cosmological constant significantly affects the parameter space. We also find the presence of an outer separatrix, which further constrains the region of bound orbits; outside this boundary, the cosmological term dominates, rendering orbits unstable.

For the dissipative effects, we use the prescription by Hoque and Aggarwal to compute the post-Newtonian gravitational fluxes for a binary system influenced by the cosmological constant. We show that the cosmological constant increases the rate of decay of the orbital parameters when translated into radiation reaction equations. Due to the increase in Keplerian binding energy and angular momentum, the cosmological constant introduces new dynamical effects in the radiation reaction. While the cosmological constant generally reduces the rate of orbital decay compared to standard post-Newtonian radiation reaction in flat spacetime, we find a nontrivial increase in eccentricity evolution at initially low eccentricities. We attribute this to the non-trivial coupling of the cosmological constant with eccentricity, where binaries with nonzero eccentricity are more sensitive to its effects.

We have investigated the effect of the cosmological constant on physical quantities such as circularization, plunge times, and orbital trajectories. Deviations from post-Newtonian orbital shapes are observed for eccentric binaries. We also generate waveforms produced by binaries under radiation reaction, showing an increase in amplitude and phase advance due to the cosmological constant. The phase advance is linked to a decrease in orbital frequency, also caused by the cosmological constant. Finally, we calculate the detection timescales for these waveforms, demonstrating that the cosmological constant increases the number of detectable sources within a given time.

Although the contribution from  $\Lambda$  is typically subleading compared to dominant post-Newtonian terms, we see a relative importance growing in certain regions of the parameter space (where the cosmological repulsion might be dominant over the radiation reaction dynamics) where it could become comparable in magnitude. Again, our results may be interpreted more generally as describing a quadratic term to the effective gravitational potential,  $\delta V \sim \Lambda r^2$ , with  $\Lambda$  serving as an effective parameter for environmental perturbations exhibiting the same scaling. The formalism developed here therefore extends beyond the purely cosmological context, providing a unified framework for analyzing systems subject to  $r^2$  corrections to the effective potential and clarifying their combined conservative and radiation-reaction–driven evolution.

Lastly, we are currently extending our investigation of the cosmological constant’s effects on radiation reaction to the strong-field regime. Additionally, much work is needed to incorporate other environmental effects from realistic astrophysical scenarios. Future studies may explore cases with non-constant cosmic acceleration, such as in the McVittie black hole spacetime [87], which we leave for subsequent research.

## Acknowledgements

The authors would like to thank Niels Warburton and Reggie Bernardo for helpful correspondence on the draft and also the organizers of the 27th Capra Meeting on Radiation Reaction in General Relativity, held at the National University of Singapore where this project was

presented. We would also like to thank Jezreel Castillo, Sean Fortuna, Jerome Mecca, Delo Procurato, and Jane BDM Garcia for help with the numerics and visualizations in the paper. This work was made possible by the support of the University of the Philippines Diliman OVPAA through Grant No. OVPAA-BPhD-2016-13 and the University of the Philippines Diliman OVCRD through Project No. 191937 ORG. JAN Villanueva would like to thank DOST ASTHRDP Scholarship for funding their PhD program in the University of the Philippines Diliman.

## References

- [1] R. Abbott, T. Abbott, F. Acernese, K. Ackley, C. Adams, N. Adhikari et al., *Gwtc-3: Compact binary coalescences observed by ligo and virgo during the second part of the third observing run*, *Physical Review X* **13** (2023) 041039.
- [2] M. Branchesi, *Multi-messenger astronomy: gravitational waves, neutrinos, photons, and cosmic rays*, in *Journal of Physics: Conference Series*, vol. 718, p. 022004, IOP Publishing, 2016, DOI.
- [3] P. Mészáros, D.B. Fox, C. Hanna and K. Murase, *Multi-messenger astrophysics*, *Nature Reviews Physics* **1** (2019) 585.
- [4] A. Palmese, R. Kaur, A. Hajela, R. Margutti, A. McDowell and A. MacFadyen, *Standard siren measurement of the hubble constant using gw170817 and the latest observations of the electromagnetic counterpart afterglow*, *Physical Review D* **109** (2024) 063508.
- [5] S.M. Carroll, *The cosmological constant*, *Living reviews in relativity* **4** (2001) 1.
- [6] P.J.E. Peebles and B. Ratra, *The cosmological constant and dark energy*, *Reviews of modern physics* **75** (2003) 559.
- [7] N. Aghanim, Y. Akrami, F. Arroja, M. Ashdown, J. Aumont, C. Baccigalupi et al., *Planck 2018 results-i. overview and the cosmological legacy of planck*, *Astronomy & Astrophysics* **641** (2020) A1.
- [8] N. Seto and K. Kyutoku, *Prospects of the local hubble parameter measurement using gravitational waves from double neutron stars*, *Monthly Notices of the Royal Astronomical Society* **475** (2018) 4133.
- [9] D.E. Holz and S.A. Hughes, *Using gravitational-wave standard sirens*, *The Astrophysical Journal* **629** (2005) 15.
- [10] S.M. Feeney, H.V. Peiris, A.R. Williamson, S.M. Nissanke, D.J. Mortlock, J. Alsing et al., *Prospects for resolving the hubble constant tension with standard sirens*, *Physical review letters* **122** (2019) 061105.
- [11] N. Tamanini, C. Caprini, E. Barausse, A. Sesana, A. Klein and A. Petiteau, *Science with the space-based interferometer elisa. iii: Probing the expansion of the universe using gravitational wave standard sirens*, *Journal of Cosmology and Astroparticle Physics* **2016** (2016) 002.
- [12] J. Roulet and M. Zaldarriaga, *Constraints on binary black hole populations from ligo-virgo detections*, *Monthly Notices of the Royal Astronomical Society* **484** (2019) 4216.
- [13] K. Siellez, M. Boer and B. Gendre, *Simultaneous event detection rates by electromagnetic and gravitational wave detectors in the advanced era of ligo and virgo*, *Monthly Notices of the Royal Astronomical Society* **437** (2014) 649.
- [14] N. Tamanini, *Late time cosmology with lisa: probing the cosmic expansion with massive black hole binary mergers as standard sirens*, in *J. Phys. Conf. Ser.*, vol. 840, p. 012029, 2017, DOI.
- [15] W. Del Pozzo, A. Sesana and A. Klein, *Stellar binary black holes in the lisa band: a new class of standard sirens*, *Monthly Notices of the Royal Astronomical Society* **475** (2018) 3485.

[16] K. Arun, E. Belgacem, R. Benkel, L. Bernard, E. Berti, G. Bertone et al., *New horizons for fundamental physics with lisa*, *Living Reviews in Relativity* **25** (2022) 4.

[17] M. Colpi, K. Danzmann, M. Hewitson, K. Holley-Bockelmann, P. Jetzer, G. Nelemans et al., *Lisa definition study report*, *arXiv preprint arXiv:2402.07571* (2024) .

[18] P. Amaro-Seoane, H. Audley, S. Babak, J. Baker, E. Barausse, P. Bender et al., *Laser interferometer space antenna*, *arXiv preprint arXiv:1702.00786* (2017) .

[19] N. Karnesis, N. Stergioulas, G. Pappas, C. Anastopoulos, J. Antoniadis, T. Apostolatos et al., *The laser interferometer space antenna mission in greece white paper*, *International Journal of Modern Physics D* **33** (2024) 2450027.

[20] E. Barausse, E. Berti, T. Hertog, S.A. Hughes, P. Jetzer, P. Pani et al., *Prospects for fundamental physics with lisa*, *General Relativity and Gravitation* **52** (2020) 1.

[21] P. Amaro-Seoane, J. Andrews, M. Arca Sedda, A. Askar, Q. Baghi, R. Balasov et al., *Astrophysics with the laser interferometer space antenna*, *Living Reviews in Relativity* **26** (2023) 2.

[22] E. Barausse, V. Cardoso and P. Pani, *Can environmental effects spoil precision gravitational-wave astrophysics?*, *Physical Review D* **89** (2014) 104059.

[23] A. Toubiana, L. Sberna, A. Caputo, G. Cusin, S. Marsat, K. Jani et al., *Detectable environmental effects in gw190521-like black-hole binaries with lisa*, *Physical review letters* **126** (2021) 101105.

[24] L. Zwick, P.R. Capelo and L. Mayer, *Priorities in gravitational waveforms for future space-borne detectors: vacuum accuracy or environment?*, *Monthly Notices of the Royal Astronomical Society* **521** (2023) 4645.

[25] G. Caneva Santoro, S. Roy, R. Vicente, M. Haney, O.J. Piccinni, W. Del Pozzo et al., *First constraints on compact binary environments from ligo-virgo data*, *Physical Review Letters* **132** (2024) 251401.

[26] E. Barausse, *Relativistic dynamical friction in a collisional fluid*, *Monthly Notices of the Royal Astronomical Society* **382** (2007) 826.

[27] C.F. Macedo, P. Pani, V. Cardoso and L.C. Crispino, *Into the lair: gravitational-wave signatures of dark matter*, *The Astrophysical Journal* **774** (2013) 48.

[28] E. Barausse and L. Rezzolla, *Influence of the hydrodynamic drag from an accretion torus on extreme mass-ratio inspirals*, *Physical Review D* **77** (2008) 104027.

[29] V. Cardoso and F. Duque, *Environmental effects in gravitational-wave physics: Tidal deformability of black holes immersed in matter*, *Physical Review D* **101** (2020) 064028.

[30] R. Eatough, H. Falcke, R. Karuppusamy, K. Lee, D. Champion, E. Keane et al., *A strong magnetic field around the supermassive black hole at the centre of the galaxy*, *Nature* **501** (2013) 391.

[31] V.P. Frolov, *Motion of a rotating black hole in a homogeneous electromagnetic field*, *Physical Review D* **109** (2024) 064045.

[32] B. Bonga and J.S. Hazboun, *Power radiated by a binary system in a de sitter universe*, *Physical Review D* **96** (2017) 064018.

[33] S.J. Hoque and A. Aggarwal, *Quadrupolar power radiation by a binary system in de sitter background*, *International Journal of Modern Physics D* **28** (2019) 1950025.

[34] Z. Stuchlk and S. Hledk, *Some properties of the schwarzschild-de sitter and schwarzschild-anti-de sitter spacetimes*, *Physical Review D* **60** (1999) 044006.

[35] Z. Stuchlk, *The motion of test particles in black-hole backgrounds with non-zero cosmological constant*, *Bulletin of the Astronomical Institutes of Czechoslovakia* **34** (1983) 129.

[36] E. Hackmann and C. Lämmerzahl, *Complete analytic solution of the geodesic equation in schwarzchild-(anti-) de sitter spacetimes*, *Physical review letters* **100** (2008) 171101.

[37] A. Ashtekar, B. Bonga and A. Kesavan, *Asymptotics with a positive cosmological constant: I. basic framework*, *Classical and Quantum Gravity* **32** (2014) 025004.

[38] A. Ashtekar, B. Bonga and A. Kesavan, *Gravitational waves from isolated systems: Surprising consequences of a positive cosmological constant*, *Physical review letters* **116** (2016) 051101.

[39] N.T. Bishop, *Gravitational waves in a de sitter universe*, *Physical Review D* **93** (2016) 044025.

[40] A. Ashtekar, *Implications of a positive cosmological constant for general relativity*, *Reports on Progress in Physics* **80** (2017) 102901.

[41] A. Ashtekar, B. Bonga and A. Kesavan, *Asymptotics with a positive cosmological constant. ii. linear fields on de sitter spacetime*, *Physical Review D* **92** (2015) 044011.

[42] A. Ashtekar, B. Bonga and A. Kesavan, *Asymptotics with a positive cosmological constant. iii. the quadrupole formula*, *Physical Review D* **92** (2015) 104032.

[43] G. Date and S.J. Hoque, *Gravitational waves from compact sources in a de sitter background*, *Physical Review D* **94** (2016) 064039.

[44] G. Date and S.J. Hoque, *Cosmological horizon and the quadrupole formula in de sitter background*, *Physical Review D* **96** (2017) 044026.

[45] S.J. Hoque and A. Virmani, *On propagation of energy flux in de sitter spacetime*, *General Relativity and Gravitation* **50** (2018) 40.

[46] B. Bonga, C. Bunster and A. Pérez, *Gravitational radiation with  $\lambda > 0$* , *Physical Review D* **108** (2023) 064039.

[47] F. Kottler, *The physical basis of einstein's theory of gravitation*, *Ann. Phys.(Leipzig)* **56** (1918) 401.

[48] J. Frank, A. King, D. Raine et al., *Accretion power in astrophysics*, Cambridge university press (2002).

[49] B. Preston and E. Poisson, *Light-cone gauge for black-hole perturbation theory*, *Physical Review D—Particles, Fields, Gravitation, and Cosmology* **74** (2006) 064010.

[50] R. Konoplya, *Particle motion around magnetized black holes: Preston-poisson space-time*, *Physical Review D—Particles, Fields, Gravitation, and Cosmology* **74** (2006) 124015.

[51] W. De Sitter, *On einstein's theory of gravitation and its astronomical consequences. second paper*, *Monthly notices of the royal astronomical society* **77** (1916) 155.

[52] G.C. McVittie, *General relativity and cosmology* , .

[53] D. Scolnic, A.G. Riess, Y.S. Murakami, E.R. Peterson, D. Brout, M. Acevedo et al., *The hubble tension in our own backyard: Desi and the nearness of the coma cluster*, *The Astrophysical Journal Letters* **979** (2025) L9.

[54] L. Dai and R. Blandford, *Roche accretion of stars close to massive black holes*, *Monthly Notices of the Royal Astronomical Society* **434** (2013) 2948.

[55] O. Yanchyshen and C. Lämmerzahl, *Gaussian orbital perturbation theory in schwarzchild space-time in terms of elliptic functions*, *Classical and Quantum Gravity* **42** (2025) 045010.

[56] C. Cutler, D. Kennefick and E. Poisson, *Gravitational radiation reaction for bound motion around a Schwarzschild black hole*, *Physical Review D* **50** (1994) 3816.

[57] J.B. Hartle, *Gravity: An introduction to einstein's general relativity*, 2003.

[58] S.L. Shapiro and S.A. Teukolsky, *Black holes, white dwarfs, and neutron stars: The physics of compact objects*, John Wiley & Sons (2008).

[59] S.M. Carroll, *Spacetime and geometry*, Cambridge University Press (2019).

[60] P. Amaro-Seoane, C.F. Sopuerta and M.D. Freitag, *The role of the supermassive black hole spin in the estimation of the emri event rate*, *Monthly Notices of the Royal Astronomical Society* **429** (2013) 3155.

[61] S. Suzuki and K.-i. Maeda, *Innermost stable circular orbit of a spinning particle in kerr spacetime*, *Physical Review D* **58** (1998) 023005.

[62] J. Levin and G. Perez-Giz, *Homoclinic orbits around spinning black holes. i. exact solution for the kerr separatrix*, *Physical Review D* **79** (2009) 124013.

[63] L.C. Stein and N. Warburton, *Location of the last stable orbit in kerr spacetime*, *Physical Review D* **101** (2020) 064007.

[64] D. Pugliese, H. Quevedo and R. Ruffini, *Motion of charged test particles in reissner-nordström spacetime*, *Physical Review D* **83** (2011) 104052.

[65] V. Misra and J. Levin, *Rational orbits around charged black holes*, *Physical Review D* **82** (2010) 083001.

[66] E. Hackmann and H. Xu, *Charged particle motion in kerr-newmann space-times*, *Physical Review D* **87** (2013) 124030.

[67] D. Kunst, V. Perlick and C. Lämmerzahl, *Isofrequency pairing of spinning particles in schwarzschild-de sitter spacetime*, *Physical Review D* **92** (2015) 024029.

[68] Y.-P. Zhang, S.-W. Wei, P. Amaro-Seoane, J. Yang and Y.-X. Liu, *Motion deviation of test body induced by spin and cosmological constant in extreme mass ratio inspiral binary system*, *The European Physical Journal C* **79** (2019) 856.

[69] C.M. Bender and S.A. Orszag, *Advanced mathematical methods for scientists and engineers I: Asymptotic methods and perturbation theory*, Springer Science & Business Media (2013).

[70] S.J. Hoque and A. Aggarwal, *Quadrupolar power radiation by a binary system in de sitter background*, *International Journal of Modern Physics D* **28** (2019) 1950025.

[71] M. Maggiore, *Gravitational waves: Volume 1: Theory and experiments*, vol. 1, Oxford University Press (2008).

[72] P.C. Peters, *Gravitational radiation and the motion of two point masses*, *Physical Review* **136** (1964) B1224.

[73] A. Pound and E. Poisson, *Osculating orbits in schwarzschild spacetime, with an application to extreme mass-ratio inspirals*, *Physical Review D—Particles, Fields, Gravitation, and Cosmology* **77** (2008) 044013.

[74] E. Poisson and C.M. Will, *Gravity: Newtonian, post-newtonian, relativistic*, Cambridge University Press (2014).

[75] K. Martel, *Gravitational waveforms from a point particle orbiting a schwarzschild black hole*, *Physical Review D* **69** (2004) 044025.

[76] K. Martel and E. Poisson, *Gravitational perturbations of the schwarzschild spacetime: a practical covariant and gauge-invariant formalism*, *Physical Review D* **71** (2005) 104003.

[77] S. Hopper and C.R. Evans, *Gravitational perturbations and metric reconstruction: Method of extended homogeneous solutions applied to eccentric orbits on a schwarzschild black hole*, *Physical Review D* **82** (2010) 084010.

[78] L.B. Szabados and P. Tod, *A review of total energy-momenta in gr with a positive cosmological constant*, *International Journal of Modern Physics D* **28** (2019) 1930003.

[79] S.J. Hoque, S.P. Kashyap, A. Virmani et al., *de sitter teukolsky waves*, *Classical and Quantum Gravity* **41** (2024) 225011.

- [80] G. Compère, S.J. Hoque and E.S. Kutluk, *So (1, 4) flux-balance laws of de sitter spacetime at quadrupolar order*, *Physical Review D* **111** (2025) 064039.
- [81] S.A. Teukolsky, *Linearized quadrupole waves in general relativity and the motion of test particles*, *Physical Review D* **26** (1982) 745.
- [82] X. He, J. Jing and Z. Cao, *Relationship between bondi-sachs quantities and source of gravitational radiation in asymptotically de sitter spacetime*, *International Journal of Modern Physics D* **27** (2018) 1850046.
- [83] A. Pound, E. Poisson and B.G. Nickel, *Limitations of the adiabatic approximation to the gravitational self-force*, *Physical Review D* **72** (2005) 124001.
- [84] P. Amaro-Seoane, J.R. Gair, M. Freitag, M.C. Miller, I. Mandel, C.J. Cutler et al., *Intermediate and extreme mass-ratio inspirals—astrophysics, science applications and detection using lisa*, *Classical and Quantum Gravity* **24** (2007) R113.
- [85] P. Amaro-Seoane, *Relativistic dynamics and extreme mass ratio inspirals*, *Living reviews in relativity* **21** (2018) 4.
- [86] P.A. Ade, N. Aghanim, M. Arnaud, M. Ashdown, J. Aumont, C. Baccigalupi et al., *Planck 2015 results-xiii. cosmological parameters*, *Astronomy & Astrophysics* **594** (2016) A13.
- [87] B.C. Nolan, *Particle and photon orbits in mcvittie spacetimes*, *Classical and Quantum Gravity* **31** (2014) 235008.